

**“BiFeO₃ (BFO) BASED PHOTO ELECTRODE FOR SUPERIOR
PHOTOELECTROCHEMICAL WATER SPLITTING”**

A Project Report Submitted to



**Tuljaram Chaturchand College of Arts, Science and Commerce, Baramati
(Autonomous)**

Under

‘Seed Money for Teacher Scheme’

Submitted by

Principal Investigator

PROF. DR. ASHOK EKNATH KALANGE

Co-Investigator

Dr. Sachin B. Kulkarni and Mr. Sopan M. Thorat

Department of Physics

Year 2023-24

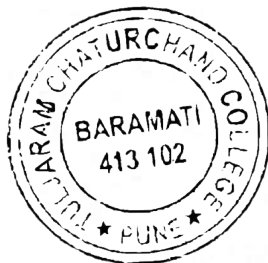
CERTIFICATE

This is to certify that the final report on a research project Seed Money for Teacher Scheme 2023-24 entitled, "**BiFeO₃ (BFO) Based Photo Electrode For Superior Photoelectrochemical Water Splitting**" is a record of bonafide research work carried out by Principal investigator Mr. Ashok Eknath Kalange and Co-Investigator Dr. Sachin B Kulkarni and Mr. Sopan M Thorat, Department of Physics, Tuljaram Chaturchand College of Arts, Science and Commerce, Baramati (Autonomous) Dist-Pune, Maharashtra.

A copy of the final report of Research Project has been kept in the library of college and an executive summary of the report has been posted on the website of the college.


Principal

Dr. Avinash S. Jagtap



DECLARATION

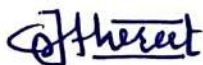
I hereby declare that the project report entitled, "**BiFeO₃ (BFO) Based Photo Electrode For Superior Photoelectrochemical Water Splitting**" completed and written by me under the financial support of Seed Money for Teacher Scheme 2023-24, at Tuljaram Chaturchand College of Arts, Science and Commerce, Baramati (Autonomous) Dist-Pune, Maharashtra have not been previously published or formed the basis of any degree, diploma, research project or any other similar title.

Place: Baramati

Date:



Co-Investigator- i) Dr.S.B. Kulkarni



ii) Mr. S. M. Thorat



Prof. Dr. A.E. Kalange

Principal Investigator




ACKNOWLEDGMENTS


It is my privilege to express sincere thanks to Hon. Prof. Dr. Avinash S. Jagtap, the Principal of Tuljaram Chaturchand College of Arts, Science and Commerce, Baramati, for providing me the necessary facilities and sanctioned funding amount (Seed Money) for research work. I am sincerely thankful to Dr. S. B. Kulkarni, CIAR Director and Dr. S. T. Salunke, Assistant Professor and ARC Chairman of T. C. College, Baramati, giving me the golden opportunity to undergo the research programme in the college of excellence.

Also my sincere thanks to Mr. Y.B. Walake, Lab assistants, Department of Physics, our college and non-teaching staff, Mr. D. D. Jamdade, for their timely help during my research work.

Last but not least I would like to express my great sense of gratitude to all the well-wishers who directly or indirectly helped me during this entire research work.


Co-Investigator- i) Dr. S.B. Kulkarni


ii) Mr. S. M. Thorat


Prof. Dr. A.E. Kalange
Principal Investigator



Index

Sr. No.	Chapter No.	Content	Page No.
1.	Chapter - I	Introduction	6
2.	Chapter -II	Review of Literature	11
3.	Chapter - III	Materials and Method	30
4.	Chapter - IV	Results and Discussion	44
5.	Chapter - V	Summery and Conclusion	50

Chapter - I

Introduction

Generation of solar energy using wide spectrum responsive photocatalyst is a foremost “green solution” to assemble the fast increase in energy demands of an enhancing global population. The most frequently used materials for photocatalytic water splitting are the transition metal oxides with band-gaps (>3.0 eV) are too high to used as efficient photocatalysts under visible light irradiation. In order to overcome this difficulty, a large number of steps have been taken to reduce their band- gap to increase their visible response, mainly through doping like nitrogen, sulfur. The other way is, through coupling with visible light responsive molecular catalysts or dyes. The search for stable, efficient, low cost photocatalysts for the slow four electron process of oxidation of water is regarded to be a major barrier for the introduction of large-scale water spitting devices. Recombination of electron-hole pairs is another limiting factor over efficiency.

However a vital solution is the use of a photoelectrochemical (PEC) cell, wherein an external voltage can efficiently separate the photo-generated charge carriers. Perovskite bismuth ferrite (BiFeO_3 i.e. BFO) has a direct band-gap of ~ 2.2 eV and is a potential multifunctional material that also exhibits multiferroic nature and photocatalytic properties. The BFO has been demonstrated to be a promising oxygen evolution photocatalyst having high efficiencies under both UV- and visible light irradiation.

To build up clean and renewable energy from sunlight is projected to meet the critical necessities for societal sustainable development. We are mainly focuses on reactions that might be useful for maintaining our environment, which includes hydrogen production, carbon dioxide reduction and to reduce the various destructive pollutants. The total amount of solar energy impinging on the earth's surface in year is about 3×10^{24} J. By considering the increasing demand of energy and to control global warming, it is important to search an efficient conversion of solar energy into other useful forms is one of the most important challenges for future research and technology development. To design a system for the purpose of converting solar energy into chemical or electricity, two criterions must be use. The first is absorption of solar illumination by some chemical substance, which leads to the creation of electrons and holes. The second one is the effective separation of these electron-hole pairs with little energetic loss before they recombine with other holes or electrons. The efficient use of solar energy could improve many energy and environmental issues. One of the efficient ways is to use hydrogen as an energy or energy carrier, since its utilization process does not produce destructive pollutants or green house gases, particularly when the

fuel cell is used as a hydrogen energy converter. However, a wide use of hydrogen as a new energy source is still facing lot of problems, namely the lack of naturally available diatomic H_2 and the absence of efficient hydrogen storage technology. Formation of H_2 from water splitting reaction by using solar energy as the primary energy source is promising way because it may provide a solution for the environmental degradation. Photoelectrochemical (PEC) water splitting technology is of meticulous concern, which converts light energy into chemical and electrical energies. Overall power conversion efficiency in PEC cells is restricted due to light absorption and fast carrier combination.

The use of water splitting for the production of hydrogen is largely used since, the Fujishima et al, discovered that the n-type TiO_2 photo electrochemical (PEC) electrode can split water to produce hydrogen by irradiation of sunlight. However much work has been carried out on different types of semiconductors such as ZnO , Fe_2O_3 and WO_3 , as photo catalysts to produce H_2 from water splitting. Among different types of photo catalysts mentioned above, TiO_2 can be mostly investigated material for photo catalytic hydrogen generation from water splitting due to its easy availability and good chemical stability. In recent years, perovskite bismuth ferrite ($BiFeO_3$, often denoted as BFO) has been considered as a promising, well known multiferroic material which shows simultaneously magnetic and electric ordering. Recently, bismuth ferrites have been attracted a great of interest for water splitting and considered as a promising visible light driven photocatalyst for degradation of destructive pollutants, due to its narrow band gap (~ 2.2 eV) which makes them to allow visible light photo catalytic activity.

• Fundamental theory of photocatalytic water splitting

Many researchers have been extensively working on the fundamentals of photocatalysis and its application in the production of hydrogen fuel, due to its crucial necessity in solving global energy and environmental issues associated with fossil fuel. Therefore, tremendous efforts have been devoted to develop stable and efficient semiconductor-based photocatalytic materials that can absorb visible light and split water at the same time. To achieve an efficient water splitting reaction, there are many requirements to be considered when choosing the appropriate semiconductor photocatalyst material. The band gap of any semiconductor used for water splitting must be less than 3.0 eV (~ 420 nm) and greater than 1.23 eV corresponding to water splitting potential. It is worth mentioning that even semiconductors with optimized band gap can produce low efficient hydrogen due to many factors such as: 1) quick electron-hole recombination on the surface of the semiconductor or in the bulk which leads to low quantum efficiency of photocatalysis

- 2) quick back reaction of oxygen and hydrogen, and
- 3) semiconductor is unable to utilize the visible light region.

To overcome these barriers, loading noble metal on the semiconductor can solve the electron-hole recombination problem. Likewise, adding sacrificial reagents such as alkaline sodium persulfate, sodium sulfite, and many others into the reaction could improve quantum efficiency and reduce charge recombination. Solar energy, the most abundant and clean energy source which can provide massive power to meet the energy demand needed for our future. Along with the lots of solar energy methods, solar-to-hydrogen conversion is known to be a promising process where clean fuel is produced and transported with zero emission. The research and development of solar hydrogen fuel is of great interest, therefore many laboratories like National Renewable Energy Laboratory has been extensively working on hydrogen production from renewable energy source.

The PEC water splitting processes take place with several steps as follows (Fig 1)

1. Absorption of solar radiation by the photoelectrode, followed by charge carrier generation as a result of photoexcitation of electrons in the valence band of photoelectrode;
2. Separation and transport of charge carriers to the electrode surface by the internal or external bias applied through the circuit;
3. Oxidation of water at the anode by the photoexcited holes. Simultaneously, transport of H^+ ions from the anode to the cathode, and transport of the photoexcited electrons to the cathode through an external circuit, followed by the reduction of H^+ ions into hydrogen gas at the cathode by the photoexcited electrons. As a result of the series of steps in the PEC water splitting, the solar energy can be converted into the hydrogen gas as the chemical fuel. The bottleneck for the realization of efficient and practical water splitting systems lies on the way to (1) effective charge carrier generation and separation, and (2) rapid water redox kinetics. The overall process is represented in Figure 1 with the PEC water splitting system consists of the photoanode and the metal counterpart as the cathode.

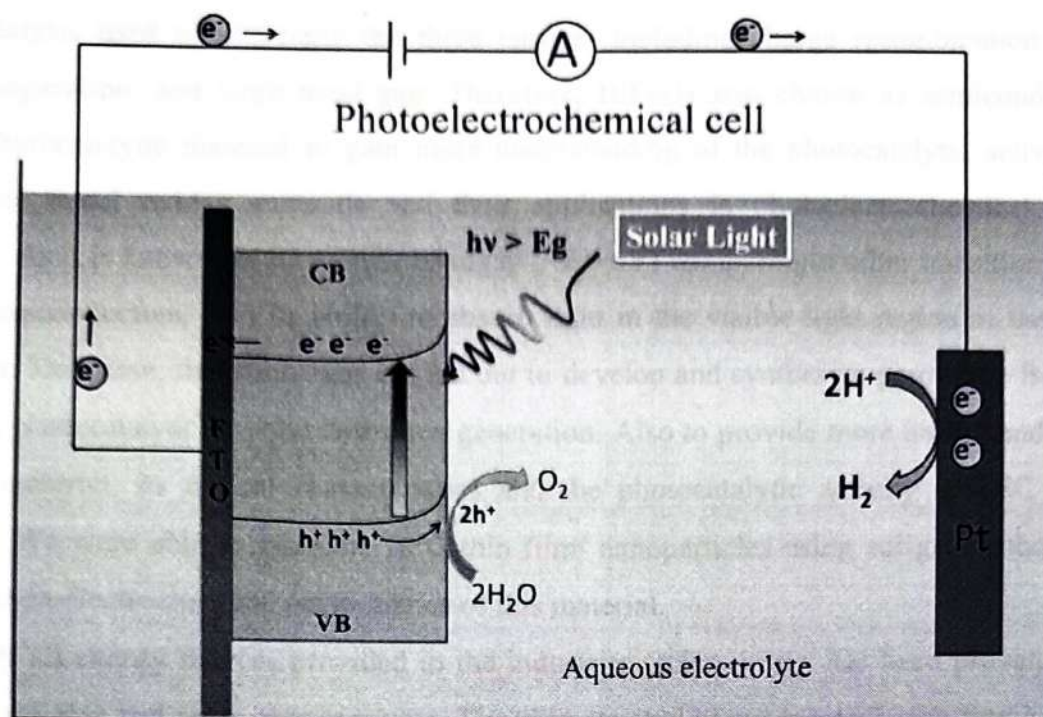


Fig 1: PEC water splitting system

Photoelectrochemical (PEC) water splitting using semiconductor-based photocatalyst is considered one of the many routes used for hydrogen fuel production. In particular, PEC water splitting is a process in which solar energy is converted into chemical energy using solar light (i.e sunlight) and water only to produce clean H_2 fuel and briefly described as follows. When a semiconductor photocatalyst is irradiated by sun light, it absorbs the photons with energy greater than the band gap (E_g).

Next, the electrons are excited to the conduction band leaving the holes in the valence band. These photo generated charge carriers separate and migrate to the surface of the photocatalyst and used as reducing and oxidizing agents to produce H_2 and O_2 respectively. In order to maintain an efficient water splitting process, the bandgap of the semiconductors should be larger than the water electrolysis potential of 1.23 eV and less than 3.0 eV to harvest visible light and possess proper band structure. Moreover, the conduction band must be lower than (0 V vs. RHE), and the valence band must be higher than (1.23 eV vs. RHE). For the semiconductor to act as photocatalyst for water splitting, it must follow certain requirements. First, the semiconductor must have a sufficiently narrow bandgap to harness visible light of the solar spectrum. Second, the ability to reduce charge recombination during the reaction. Third, maintaining high efficiency of charge separation.

Based on the above conditions, semiconductor-based materials act as promising photocatalysis used to overcome the three barriers including charge recombination, poor charge separation, and large band gap. Therefore, BiFeO_3 was chosen as semiconductor-based photocatalytic material to gain more understanding of the photocatalytic activity of perovskite metal oxides materials and their applications in photoelectrochemical water splitting. As it is known for its narrow bandgap (~ 2.0 eV) comparing to other transition metal oxide semiconductors, also its ability to absorb light in the visible light region of the solar spectrum. Therefore, this study was carried out to develop and synthesize perovskite BiFeO_3 thin film photocatalyst for solar hydrogen generation. Also to provide more understanding of BiFeO_3 material, its optical characteristics and the photocatalytic activity in PEC water splitting. We were able to fabricate BFO thin film/ nanoparticles using sol-gel method and test the photoelectrochemical performance of this material.

Of all energy sources provided in the industries, solar energy has been proven to be the most reliable and clean energy source. The ultimate goal of our research is to find a stable semiconductor material with optimum band gap used as photocatalyst to generate hydrogen fuel via photoelectrochemical water splitting. In the present study, the synthesis of BiFeO_3 and its photoelectrochemical water splitting properties will be investigated. This work will gain fundamental understanding of suitability of perovskite BFO and their composite for water splitting. The knowledge obtained will promote the application of BiFeO_3 -based thin films/ nanoparticles in solar-to-hydrogen conversion.

CHAPTER-II

REVIEW OF LITERATURE

Photoelectrochemical water splitting is an efficient way to generate valuable hydrogen by using solar light and water. Using solar energy to generate clean and efficient hydrogen through photoelectrochemical (PEC) water splitting will make a momentous contribution towards mankind's goal of reducing GHG emissions worldwide [1-3]. In 1972 Fujishima and Honda verified PEC water splitting by TiO_2 , which has attracted worldwide interest since it provides an ecofriendly approach to convert solar energy into fuels [4]. Since then remarkable efforts have been taken on developing high performance semiconductors for PEC water splitting. Although many semiconductor materials have been investigated during the past several decades, there is still no material to fulfill all the requirements in terms of efficiency and stability. Therefore, the looking at suitable materials with strong visible light absorption, good electrical conductivity, long minority charge carrier diffusion lengths and high stability to accelerate the generation of solar H_2 and O_2 by splitting water still remains open.

The strategies for increasing the hydrogen evolution can be categorized into two streams (a) increasing active sites and (b) improving electrical conductivity. To proceed the overall water splitting in a more direct and smooth manner the exposure and accessibility of active sites, vectorial electron transport capability, and release of gaseous products should be enhanced [4-1]. Increasing the active site can be obtained by plasma treatments and by reducing the layer thickness. This helps in revealing more active sites by edge exposure and by creating more defecting sites. Development in electrical conductivity or charge transportation kinetics can be attained through straining the basal plane and by doping. Another trending strategy for improving the rate of hydrogen energy is multisite catalysis. Hydrogen evolution reaction (HER) is a multistage reaction process in which the first step is so much longer and this affects the evolution rate of hydrogen. This limitation can be overcome with the help of multisite catalysis. In this process, the density of reduction or oxidizing species accumulated on the reactive site for determines the rate laws for the photoelectrochemical reaction.

2.1) Role of nanomaterials in PEC water splitting

Nanoscale sizes are comparable to carrier scattering lengths, considerably reducing the scattering rate and rising carrier collection efficiency. Nanomaterials have strong absorption coefficients due to an increase of oscillator strength, thus enabling high

conversion efficiency. The band gap of nanomaterials (QD) can be adjusted to absorb in a particular wavelength by varying size and, in principle, cover the whole solar spectrum. By adding external impurity, the electronic band structure can be controlled. Bottom-up approach of synthesis, uses smaller components to produce larger and more complex structures which are able to allow scalable synthesis of single crystal nanostructures on flexible substrates under mild conditions, leading to light weight and low cost.

Nanoparticles are the building block for photocatalyst since their mass and charge transfer is rapid and they exhibit increased light absorption and reduced light scattering. The nanoparticles can be coated on the electrode or can be dispersed in reaction medium (water) which shows enhanced photocatalytic activities. The enhancement in water splitting efficiency was observed at the semiconductor/electrolyte interface, where the metal nanoparticles were localized. This is due to the minority charge transport to the electrolyte from the electrode [5]. In an investigation, CdS nanoparticles was prepared with uniform size ranges and experimentally proven its improved photocatalytic activities as compared to bulk CdS [6].

2.2. Photoelectrode materials

2.2.1 Material requirements

The most important aspect for PEC water splitting, as mentioned in the introduction, is the choice of a suitable photoanode and/or photocathode material. An ideal water splitting photoanode and/or photocathode requires semiconductor materials that possess the following characteristics: (i) Suitable band-gap energy and band positions. Natural sunlight consists of 5% UV (300–400 nm), 43% visible (400–700 nm), and 52% infrared radiation (700–2500 nm). Therefore, appreciable light absorption in the visible region is required to increase efficiency, and this in turn depends on the band-gap of the semiconductor. As the proton reduction potential is located at 0 V vs. NHE and the O₂/H₂O potential at 1.23 V vs. NHE (pH = 0), the theoretical minimum band-gap for water splitting requires incident photons with a minimum energy of 1.23 eV, which corresponds to a wavelength of light of 1000 nm. However, when considering the thermodynamic energy losses (0.3–0.4 eV) occurring during charge carrier transportation and the overpotential requirement for acceptable surface reaction kinetics (0.4–0.6 eV), a minimum band-gap of 1.8 eV is required, corresponding to light absorption at ca. 700 nm.

The upper limit on the band-gap energy is 3.2 eV, because of the rapid drop in sunlight intensity below 390 nm according to the solar spectrum. Therefore, for a single semiconductor photoelectrode, a band-gap energy between 1.9 eV and 3.2 eV is desirable to

obtain sizable photovoltages. Theoretically, a band-gap of ca. 2.0 eV is preferred for optimal sunlight utilization, in addition to the thermodynamic band position requirements.¹³ However, in practice, it has hardly been achieved because the expected photovoltage can seldom be met. Without high photovoltages (41.61 V), even the highest current density will not solve the problem of unbiased water splitting and thus external bias or tandem devices are needed to provide the extra voltage to split water.

For other materials, such as metal sulfides, the PDIs can be different and therefore the pH dependence is more complicated¹⁴ (a diagram showing this can be found in the overall, the band positions of most semiconductors, in particular oxides, show the same pH dependence as represented by the Nernst equation, whereas the band positions are fixed with respect to the water redox potentials. Hence, the relative difference between the band positions of an oxide photocatalyst and the water redox potential is pH independent.

(ii) Efficient charge carrier separation and transportation in the semiconductor. Fast charge recombination is a major factor contributing to low STH efficiencies, and thus a strategy to promote efficient charge carrier separation and transport is required, which depends both on the intrinsic properties (hole and electron mobility) and on the extrinsic properties (crystallinity, nanostructure) of the material. (iii) Strong catalytic activity and stability. Suitably rapid surface reaction kinetics can avoid surface charge accumulation, which would otherwise lead to electron-hole recombination.

Photocorrosion is a major problem for many candidate water splitting semiconductors, in particular metal sulfides, and occurs when the photogenerated holes/electrons do not oxidise/reduce water but instead decompose the photocatalyst itself. These photocorrosion reactions depend upon the relative positions of the semiconductor band edges and the respective decomposition potentials. Anodic photocorrosion can occur if the anodic decomposition potential (E_{pd}) is above the valence band potential of the semiconductor. Conversely, cathodic photocorrosion can occur if the cathodic decomposition potential (E_{nd}) is below the conduction band of the semiconductor. Metal oxides, such as BiVO_4 and ZnO , or metal sulphides, such as MoS_2 and CdS , can easily undergo anodic photocorrosion depending on the pH of the electrolyte, since the actual values of the decomposition potentials depend upon the pH value. However, common photoanode materials such as TiO_2 and Fe_2O_3 , even though their anodic deposition potential is above the valence band potential, are thermodynamically stable because of their very slow decomposition reaction kinetics. In addition, the photoelectrode materials should be lowcost

and composed of earth-abundant elements for practical applications. This is crucial toward justifying the argument for an economical scale-up of solar-to-fuel devices.

2.2.2) Titanium dioxide (TiO₂)

TiO₂ is the most extensively used material for water splitting and hydrogen generation studies. Bulk TiO₂ is having bandgap of 3.03 eV-3.18 eV which leads to poor efficiency in the solar light absorption although its stability and low cost makes them potentially applicable in water splitting. TiO₂ nanotube is the better alternative among TiO₂ nanomaterials. In bulk TiO₂ more rapidly electron-hole recombination occurs and this leads to low quantum efficiency. In order to diminish this phenomenon, materials with small band gaps were decorated along with TiO₂.

An substitute for decorating TiO₂ with a material, black TiO₂ nanoparticles were developed, which shows more efficient photocatalytic activities [6]. The size and shape of nanoscale TiO₂ can have a major impact on the conversion efficiency. Recently, for improving the efficiency of light absorption and hydrogen generation rate nanostructured TiO₂ has major role. On comparing TiO₂ nanorod and nanowire, nanowire are efficient than nanorods [7,8]. It was observed that, there is an increased cell performance with increase in annealing temperature. This is due to development of crystalline structure which enhances the charge transport.

2.2.3) Zinc Oxide (ZnO)

ZnO nanomaterials have been extensively used in water splitting [8]. It possess an energy bandgap ~3.3 eV and optoelectronic properties similar to those of TiO₂. The photocatalytic efficiency of ZnO is low due to its weak visible light absorption and low photocatalytic quantum efficiency. Besides this, ZnO having the band gap energy of 3.37 eV and having high exciton binding energy of 60 meV at room temperature. They are having enormously high electron mobility, chemically stable and highly transparent. Hydrogen production is depending on the several factors like the morphology, electrolyte interactions and defect density. To optimize the generation, nanostructure should modify their fundamental properties through the deposition techniques and annealing.

2.3) Bismuth based semiconductors for PEC water splitting

Metal oxide-based semiconductors are broadly used to construct photoelectrode for PEC researches. However, the most stable oxides such as TiO₂[5,6], ZnO[7,8], and SnO₂[9] are wide bandgap semiconductors with only ultra-violet (UV) light (<420 nm) absorption. At the utmost only 4% of solar energy can be used for PEC water splitting [10]. In order to make use of plentiful visible light spectrum, small bandgap materials, such as WO₃[11,12] and

Fe_2O_3 [13–15] have been studied, but the quick recombination of photo-generated charge carriers in WO_3 , low electrical conductivity and short hole diffusion lengths of Fe_2O_3 have restricted their PEC performance to a great extent.

To address the associated shortcomings, numerous alteration strategies have been recognized. Nevertheless, it is still challenging to attain a remarkable efficiency with the above-mentioned materials. Recently bismuth (Bi)-based semiconductors have aroused broad interest because of their brilliant electronic structure. The valence band of Bi-based materials is composed of hybrid O 2p orbitals and Bi 6s orbitals. The Bi 6s orbitals result in a narrow bandgap and accelerate the mobility of photo-generated charges of Bi-based semiconductors [16]. The most widely studied Bi-based semiconductors include oxyhalides, BiOX ($X = \text{Cl}, \text{Br}$ and I); oxides of the aurivillius phases such as Bi_2WO_6 and Bi_2MoO_6 , and other mixed metal oxides including BiVO_4 , BiFeO_3 , Bi_2O_3 , and CuBi_2O_4 . Among all of these, most of these materials are visible light responsive with bandgaps less than 3.0 eV (Fig. 1).

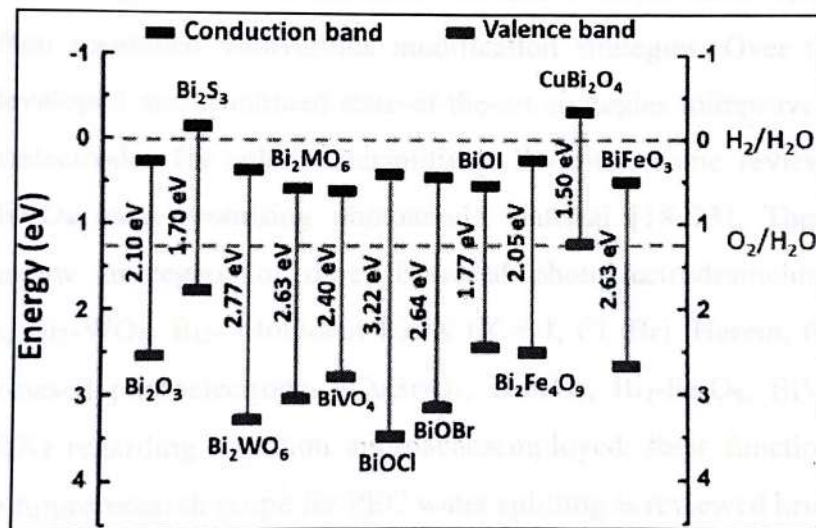


Fig 1: Band edge positions of Bi-based semiconductor photoelectrodes.

Further the visible light absorption capacity of photoelectrodes can be improved by using different modification methods [17]. The inherent optoelectronic properties of different Bi-based semiconductors, such as the band edge position, crystal structure, etc., will have some determinable power on the performance of water splitting. For example, the negative conductive band edge of CuBi_2O_4 semiconductor will result in the positive onset potential during PEC water splitting. The absorption edge listed in Table 1 reveals the approximate visible light absorption capacity of Bi-based photoelectrodes.

Bi-based photoelectrodes	Absorption edge (nm)	Ref.
CuBi ₂ O ₄	-700	[24]
BiFeO ₃	-600	[25]
Bi ₂ Fe ₄ O ₉	-600	[26]
BiVO ₄	-520	[27]
Bi ₂ WO ₆	-450	[28]
Bi ₂ MoO ₆	-450	[29]
BiOI	-615	[30]
BiOCl	-350	[31]
BiOBr	-475	[32]

Table 1: Absorption edge of different Bi-based photoelectrodes.

Inherently advantaged Bi-based materials can lead to important development in solar water splitting when combined with various modification strategies. Over the past years, researchers have developed and combined state-of-the-art strategies to improve the efficiency of Bi-based photoelectrodes for solar water splitting. Recently, some review papers have discussed about BiVO₄ as a promising photoanode material [18–23]. There still lacks a comprehensive review in regard of other Bi-based photoelectrodes including CuBi₂O₄, BiFeO₃, Bi₂Fe₄O₉, Bi₂-WO₆, Bi₂-MoO₆ and BiOX (X = I, Cl, Br). Herein, the progression associated with Bi-based photoelectrodes (CuBi₂O₄, BiFeO₃, Bi₂-Fe₄O₉, BiVO₄, Bi₂-WO₆, Bi₂-MoO₆ and BiOX) regarding variation approaches employed, their functionality, current challenges and the future research scope for PEC water splitting is reviewed briefly.

2.3.1) Copper bismuth oxide (CuBi₂O₄)

Copper bismuth oxide (CuBi₂O₄) is an intrinsic p-type semiconductor, which is likely to absorb major portion of visible light from the solar spectrum due to its suitable bandgap, ranging from 1.6 eV to 1.8 eV. Under the standard illumination of AM 1.5G illumination, the theoretical photocurrent density of this material can be over 19.7 mA cm⁻² [39–42]. In addition to this, the conduction band (CB) of CuBi₂O₄ is located at a more negative potential than the reduction potential of H⁺/H₂, allowing sufficient driving force for solar H₂ production [33–36]. Berglund et al. have made-up CuBi₂O₄ photocathode with forward gradient diffusion assisted spray pyrolysis method. In the presence of hydrogen peroxide (H₂O₂), it achieved photocurrent densities of 2.0 mA cm⁻² and 2.5 mA cm⁻² at 0.6 V vs. RHE [34,37]. Without any electron forager, a photocurrent density of 0.6 mA cm⁻² at 0.6 V

Vs RHE was achieved by doping CuBi_2O_4 photocathode with Ag dopant and loading Pt as co-catalyst [38].

Notable progress has been reported on the performance of CuBi_2O_4 photocathode in recent years. For instance, Yang et al. [39] showed that modifying CuBi_2O_4 by semi-scaled post annealing treatment can attain a photocurrent density of 0.7 mA cm^{-2} at 0.25 V vs. RHE . Li et al. [40] made-up of CuBi_2O_4 photoelectrode as a group like nanotexture, which shows a photocurrent density as high as 1.55 mA cm^{-2} at 0.5 V vs. RHE and an onset potential up to 1.0 V vs. RHE in alkaline solution (1 M NaOH). With an especially positive photocurrent onset above 1.0 V vs. RHE , CuBi_2O_4 photoelectrode has the potential to drive unaided water splitting by combining with a suitable n-type photoanode [41]. Nevertheless, the photocurrent densities reported to date is a long way from the theoretical value [39,40]. One of the possible reasons for poor PEC performance is the ineffective charge separation and transfer [40].

To address the above issue, CuBi_2O_4 was used to form a type II heterojunction with CuO as shown in Fig. 2a and b. The formation of heterojunction provided supplementary driving force to accelerate the charge separation and transfer. Therefore, a record photocurrent density of 1.87 mA cm^{-2} at 0.6 V vs. SHE was obtained in 0.1 M NaOH . Due to the striking onset potential of 1.12 V vs. SHE , the heterostructured $\text{CuBi}_2\text{O}_4/\text{CuO}$ photocathode has been arranged in parallel with CoPi/BiVO_4 photoanode to realize an unbiased water splitting system (Fig. 2c and d) [30].

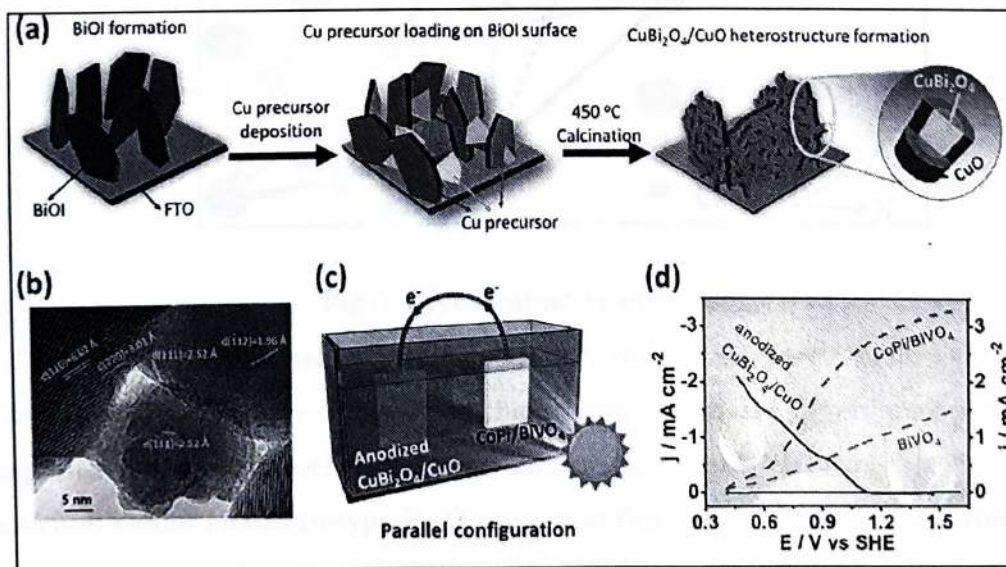


Fig 2: (a) Schematic procedures of $\text{CuBi}_2\text{O}_4/\text{CuO}$ electrode fabrication. (b) HRTEM image of the $\text{CuBi}_2\text{O}_4/\text{CuO}$ photoelectrode. (c) Schematic illustration of the parallel illuminated dual photoelectrode system. (d) j - E response of the anodized $\text{CuBi}_2\text{O}_4/\text{CuO}$ photocathode (blue

solid line), BiVO_4 (red dashed line) and Co-Pi/BiVO_4 (blue dashed line) photoanodes.

Reproduced from Ref. [30] with permission from the Royal Society of Chemistry.

2.4) Bismuth ferrite

Bismuth ferrite shows ferromagnetism, ferroelectricity and ferroelasticity which make them good materials for applications in modern electronic devices and information storage [42,43]. The most observed practical phases for bismuth ferrites are BiFeO_3 , $\text{Bi}_2\text{Fe}_4\text{O}_9$, $\text{Bi}_{25}\text{FeO}_{39}$, $\text{Bi}_{46}\text{Fe}_2\text{O}_{72}$ and $\text{Bi}_{24}\text{Fe}_2\text{O}_{39}$. The PEC water splitting has been observed only in BiFeO_3 and $\text{Bi}_2\text{Fe}_4\text{O}_9$ phases and the details related to these materials are discussed in the following section.

2.4.1. BiFeO_3

BiFeO_3 is a usual perovskite material, which exhibits ferroelectric and magnetic polarization properties [44,45]. It has rhombohedral crystal structure with space group $R3c$, where the cube-octahedral and octahedral positions are occupied by larger Bi^{3+} ions and medium sized Fe^{3+} ions, respectively (Fig.3).

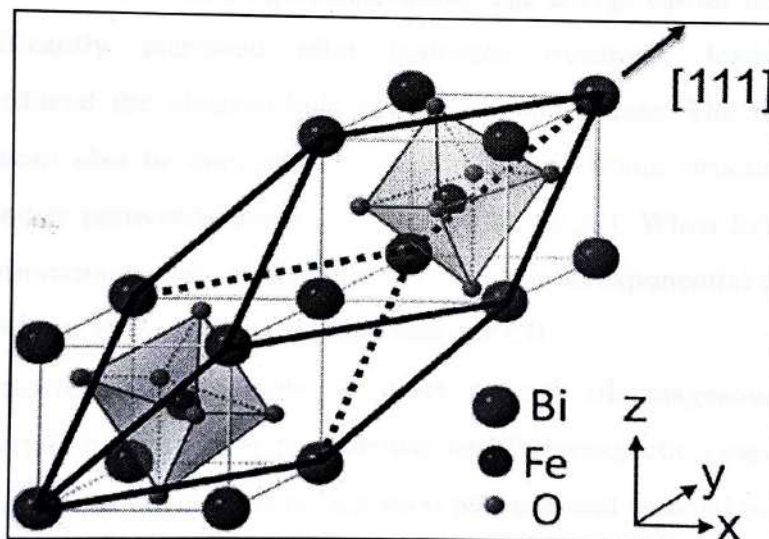


Fig 3: Crystal structure of BiFeO_3

BiFeO_3 is a direct bandgap semiconductor, which can absorb visible light up to 750 nm [46]. However, it is very difficult and challenging to form thin film of pure phase BiFeO_3 as impurity phases of Fe_2O_3 , Bi_2O_3 , $\text{Bi}_2\text{Fe}_4\text{O}_9$ are commonly present [47]. For example, parasitic iron oxides phases (α -type Fe_2O_3 or γ -type Fe_2O_3) have been detected while BiFeO_3 thin film was grown via pulsed laser deposition (PLD) method [48]. Moniz et al. [49] used ligand-matched solid organometallic precursors $[\text{Fe}(\text{OtBu})_3]_2$ and $[\text{Bi}(\text{OtBu})_3]$ to grow phase pure and high-quality BiFeO_3 thin films by low-pressure CVD (LPCVD) method. To assess

the performance of as synthesized BiFeO₃ photoanodes, PEC measurements for water oxidation were carried out.

The resultant high photocatalytic activity (0.35 mA cm⁻² at 1.23 V vs. RHE) was reasoned to the internal polarization of BiFeO₃, which improved the charge separation efficiency. Furthermore, nickel borate (Ni-B) oxygen evolution catalyst (OEC) were loaded via photo-assisted electrodeposition. It can increase the oxygen production by decreasing the over potential for water oxidation on BiFeO₃ photoelectrode. The formation of oxygen vacancies has been working to modify BiFeO₃ photoelectrode [31]. Formation of oxygen vacancy is a well-known defect engineering strategy for changing the optical properties and electronic band structures of metal oxide semiconductors. Oxygen vacancies were induced in BiFeO₃ photoelectrode by sintering the BiFeO₃ nanoparticles in hydrogen atmosphere. The hydrogen treatment improved the light absorption ability in visible region and the separation of photo-generated electron-hole pairs in oxygen deficient BiFeO₃ photoelectrode.

The optimized BiFeO₃ photoelectrode showed over three times higher photocurrent densities compared to the bare BiFeO₃ photoelectrode. The charge carrier density of BiFeO₃ photoelectrode significantly increased after hydrogen treatment, leading to improved conductivity and reduced the electron-hole pair recombination rate. The recombination of electrons and holes can also be concealed by tuning the electronic structure of BiFeO₃ by combining it with other perovskite oxides such as SrTiO₃ [50,51]. When SrTiO₃ is included with BiFeO₃, the minimum energy state of CB is raised and an exponential tail of trap states from hybridized Ti 3d and Fe 3d orbitals appears near the CB.

BiFeO₃ photoelectrode is likely to offer special advantages over conventional semiconductor materials because of its ferroelectric and ferromagnetic properties. Lei et al. [52] employed poling bias to develop its polarization property and realized both oxidation and reduction reaction using only BiFeO₃ as both a photoanode and a photocathode depending on the alignment of the field. Furthermore, BiFeO₃ plays bi-functional role when coupled with an efficient BiVO₄ [53]. This material worked as passivation coating and increased the stability of BiVO₄/BiFeO₃ significantly. Furthermore, the photocurrent density increased by 4.4 times compared to bare BiVO₄ because of proficient charge separation by BiFeO₃ passivation layer. Efficient charge separation was initiated by applying positive poling to enhance self-polarization. The self-polarization enhanced the depletion layer width by upward band bending and ensured efficient charge separation. On the contrary, PEC performance decreased after applying negative poling because of the narrowed depletion layer. The polarization

fordownward and upward band bending provides opportunities to use this single material to realize unassisted water splitting [54].

2.4.2) $\text{Bi}_2\text{Fe}_4\text{O}_9$

As compared to BiFeO_3 , $\text{Bi}_2\text{Fe}_4\text{O}_9$ has received relatively modest attention in PEC water splitting although it has excellent chemical stability, nontoxicity as well as magnetic and dielectric properties. $\text{Bi}_2\text{Fe}_4\text{O}_9$ has shown competence in photocatalytic degradation of organic pollutants in presence of visible light irradiation due to its narrow bandgap ranging from 1.9 eV to 2.1 eV [55,56]. Research work on the essential properties of $\text{Bi}_2\text{Fe}_4\text{O}_9$ for solar water splitting is greatly slowed down by the difficulty in the controllable synthesis of pure phase $\text{Bi}_2\text{Fe}_4\text{O}_9$ film [57]. Involvement of high temperature treatment, utilization of volatile organic solvents and harsh reaction conditions may cause co-existence of BiFeO_3 and $\text{Bi}_{25}\text{FeO}_{40}$ phases [58]. Briscoe et al. [57] prepare phase pure $\text{Bi}_2\text{Fe}_4\text{O}_9$ to understand its characteristics and evaluated its potential as photoanode for PEC water splitting.

However, the as-prepared photoanode shows very poor visible light harvesting ability and negligible photocurrent density of 0.05 mA cm^{-2} at 1.23 V vs. RHE. The injection hole barrier at the surface of $\text{Bi}_2\text{Fe}_4\text{O}_9$ electrode initiated the electron hole recombination and led to low photocurrent density. Compared to the first report, the photocurrent density of $\text{Bi}_2\text{Fe}_4\text{O}_9$ photoanodes significantly improved to 0.61 mA cm^{-2} at 1.23 V vs. RHE under visible light irradiation when bulk and surface modification methods were applied [32]. Oxygen vacancies were produced by nitrogen treatment (BFO-N) to modify the electrical conductivity and carrier concentration of $\text{Bi}_2\text{Fe}_4\text{O}_9$. The enhanced carrier concentration benefitted the charge separation. The charge injection obstruction was reduced by removing the surface trap states via acid treatment (HCl-BFO-N), whereas CoPi co-catalysts were loaded to promote the surface reaction kinetics. As a newly added photoanode material, $\text{Bi}_2\text{Fe}_4\text{O}_9$ deserves the attention to be modified using innovative modification strategies including nanostructuring, doping, defect engineering, constructing heterojunction and optimization in co-catalyst loading to reveal its full potential for PEC water splitting.

2.4.3) Bismuth Vanadate (BiVO_4)

There are many excellent review papers focusing on BiVO_4 , here we do not mean to discuss in details the research initiatives. In its place, we have summarized the most effective modification strategies, their functionality and the resultant photocurrents. The ability to produce visible light (bandgap 2.4 eV), appropriate valence band edge (2.6 eV vs. RHE) and stability in a wide range of aqueous media (pH 3–11) make this material attractive as a photoanode [59, 60]. Modification strategies involved such as creating nanostructure

(nanocone) [61], nanoporous [62], nanosheets [63]), doping (Mo [64], W [65]) and producing heterojunction [66] have been confirmed to efficiently increase the performance of BiVO₄. The photocurrent density has exceeded 90% (6.72 mA cm⁻²) of the theoretical maximum (7.5 mA cm⁻² based on the bandgap of 2.4 eV bandgap) by forming a core-shell heterojunction of BiVO₄/WO₃ nanorods (NRs) and further applying CoPi co-catalysts [67].

Coated BiVO₄ photoelectrode with amorphous TiO₂ also resulted in high photocurrent density through improved solar utilization and charge separation and transport [68]. Another important strategy to enhance charge separation and transfer efficiencies is to grow preferential facet oriented BiVO₄ photoelectrode [33,68]. For example, Zheng et al. achieved 16 times higher photocurrent density using a preferentially [0 0 1] oriented BiVO₄ as compared to randomly oriented BiVO₄ [69]. Lately, creating oxygen vacancies as intrinsic defects in BiVO₄ has gained popularity because oxygen vacancies can increase the charge carrier density and support charge separation in the bulk. For next-generation BiVO₄ based photoanodes is expected to design by using combination of multiple strategies where molybdenum (Mo) doped BiVO₄ was combined with boron (B) doped C₃N₄ to form heterojunction for efficient charge separation. The doped Mo can reduce the interfacial energy loss whereas the B doping in C₃N₄ could manage the work function and finally the NiFeOx OEC layer deposited NiFeOx/B-C₃N₄/Mo-BiVO₄ photoanode exhibited highest PEC water splitting performance with a moderately low bias voltage [70].

2.4.4) Bismuth tungstate (Bi₂WO₆)

Bismuth tungstate (Bi₂WO₆) is essentially rich with many different physical and chemical properties including dielectric susceptibility, ferroelectric piezoelectricity and catalytic activity [71,72]. The bandgap of this material lies in the range of 2.7–2.8 eV and has been broadly used in photocatalytic degradation of different dyes [34]. Recently, Bi₂WO₆ has been considered as a potential candidate for CO₂ reduction [73,74] and PEC water splitting [34,75]. Similar to BiFeO₃, this material is particularly interesting for PEC water splitting since it can be used as photoanode and photocathode for OER and HER, respectively by switching the charge transfer direction due to its ferroelectric polarization characteristic.

In Fig.3, it shows the mechanism to activate the bi-functional Bi₂WO₆ photoelectrode for PEC water splitting induced by charged domain walls and in-plane polarization [76]. Upon light illumination on heterostructured SrRuO₃/Bi₂WO₆ photo electrode, the photo-generated charge carriers separate at different in-plane domains because of internal polarization and gather in the charged domain wall via polarization screening. The presence of negative charges

at tail-to-tail charged domain wall causes an upward bandbending whereas the electrons are transferred to SrRuO₃ (Fig. 3a).

The upward band bending helps to migrate the holes to the surface and facilitated OER reaction. On the other hand, the positive charges at the head-to-head charged domain wall resulted in downward band bending, which accelerates the transportation of electron to facilitate HER and the holes are driven away to SrRuO₃ (Fig. 3b). The obtained anodic and cathodic photocurrent using this bi-functional ferroelectric photoelectrode was 0.175 and 0.24 mA cm⁻² at 1.23 and 0 V vs. RHE, respectively. To understand the limiting factor, a DFT study has been carried out regarding the charge carrier dynamics in Bi₂WO₆[77]. The electron transport is found to be slower compared to metal oxides such as BiVO₄, WO₃ and Fe₂O₃. This is because the CB is confined to the (WO₄²⁻) planes for the layered structure of Bi₂WO₆ and this slows down the mobility of the electron specifically in the vertical direction of CB (Fig. 3e).

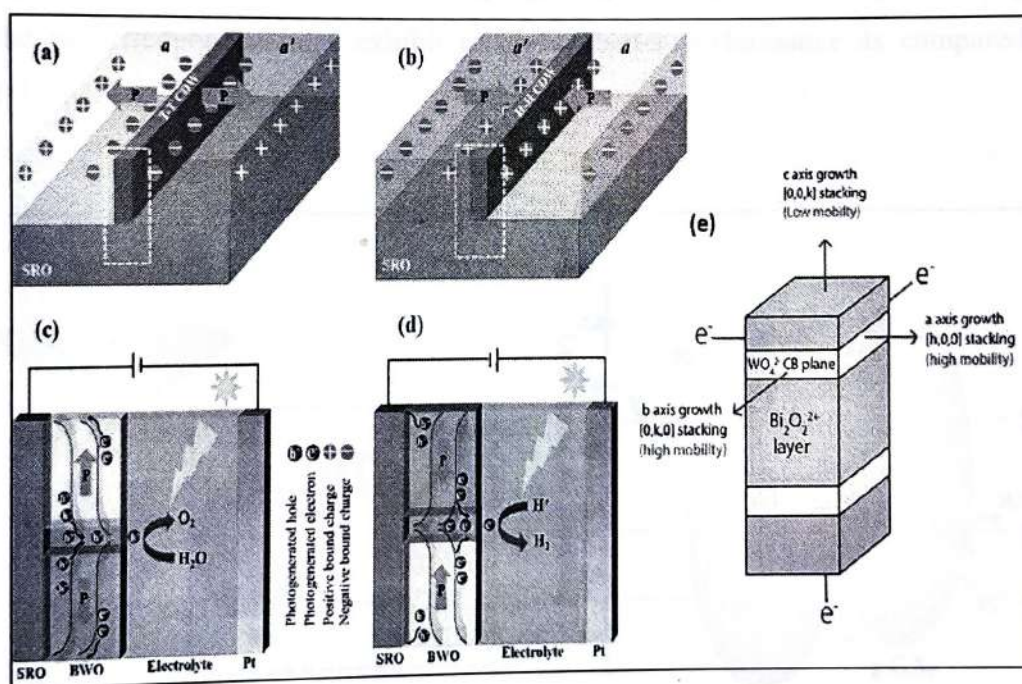


Fig. 3. Schematic of PEC water splitting activity of Bi₂WO₆ photoelectrode. Panels (a) and (b) represent the SrRuO₃/Bi₂WO₆ heterostructure with tail-to-tail (T-T) and head-to-head (H-H) charged domain walls, respectively. Panels (c) and (d) show the schematic of the water splitting mechanism as the photoanode and photocathode, respectively. Reproduced from Ref. [76] with permission from the American Chemical Society. (e) Schematic of the layered orthorhombic unit cell of Bi₂WO₆ illustrating the connection between electron transport and

preferred growth arising from a CB limited to planes in material Reproduced from Ref. [78] with permission from the American Chemical Society.

2.4.5. Bismuth molybdate (Bi_2MoO_6)

Bi_2MoO_6 belongs to aurivillius oxide family and having a layered structure where MoO_6 octahedra are sandwiched between $[\text{Bi}_2\text{O}_2]^{2+}$ layers. The reported bandgap of Bi_2MoO_6 is ~ 2.7 eV, which falls nearly in the visible region. It has shown attractive photocatalytic activity for degradation of organic pollutants and dyes [35]. Kudo et al. [80] first demonstrated its capability as O_2 evolving photocatalyst and discovered that the corner-sharing unit of MoO_6 octahedra provided a channel for photo-generated charge carriers to travel easily and contribute to photocatalytic performance, like to WO_3 photocatalysts. Lei et al. [82] constructed Bi_2MoO_6 photoanodes with vertically aligned nanowall but the photocurrent is still low showing low charge separation efficiency and severe bulk recombination. The extra driving force was provided to progress the charge separation by combining Bi_2MoO_6 photoanodes with WO_3 [82], TiO_2 [83], $\text{Bi}_2\text{Mo}_2\text{O}_9$ and $\text{g-C}_3\text{N}_4$ (Fig. 4 (a, b) and the modified photoanodes exhibit relatively better performance as compared to as prepared Bi_2MoO_6 photoanodes.

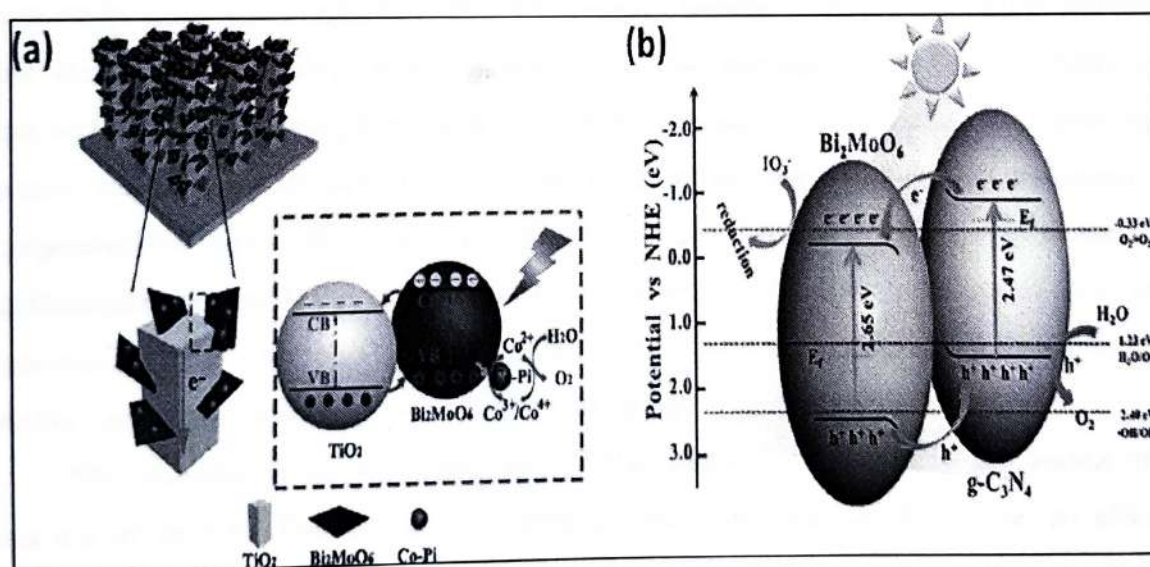


Fig 4: (a) Schematic of heterostructure of $\text{TiO}_2/\text{Bi}_2\text{MoO}_6$ and proposed mechanism for PEC water oxidation (b) Schematic of energy band structure of $\text{Bi}_2\text{MoO}_6/\text{g-C}_3\text{N}_4$ and charge transport mechanism.

2.5) Stability of Bi-based photoelectrodes

Permanence of photoelectrodes is critically important for the PEC system to be accepted as dependable energy conversion system. Many capable semiconductor candidates with excellent light harvesting capability have poor stability, which limits their utility to be

used as photoelectrode in PEC system. For example, CuBi_2O_4 has gained interest in recent years because of its specially positive onset potential but the copper-based oxides usually are slowed down by corrosion due to reduction of Cu^{2+} to Cu^+ .

Recent efforts have been noticed to enhance the stability of CuBi_2O_4 photocathodes. Jin et al. [79] applied P_{25} protective layer by spin coating on heterostructure of $\text{CuBi}_2\text{O}_4/\text{ZnSe}$ to avoid the direct contact with the electrolyte. The P_{25} protective layer protects the corrosion of Cu^{2+} and stability of the composite photocathode prolonged to 5000 s. The highest stability of CuBi_2O_4 photoelectrode without any protection layer is observed to be 5 h. The photoelectrodes were formed by depositing Bi_2O_3 and CuO layers sequentially by PLD and followed by RTP. Iron based oxides consisted of earth abundant elements are more resistant to corrosion. For BiFeO_3 based photoelectrode ($\text{BFO}/\text{75-STO}/\text{25}/\text{Pt}$), the photocurrent is remain constant for at least 12 hours under continuous irradiation at 0 V vs. RHE in phosphate solution (pH 12) [67]. $\text{Ni-B}/\text{BiFeO}_3$ photoelectrode found to be stable under operating conditions for over 3 h for both oxygen and hydrogen evolution [65].

Both as prepared and modified (bulk and surface engineered) $\text{Bi}_2\text{Fe}_4\text{O}_9$ photoanodes have been reported to retain 90% photocurrent for more than 4 hours under illumination. Among all the Bi-based photoelectrodes, BiVO_4 photoanode has achieved enormously long-term stability to date. For instance, Domen et al. [79] exhibited stability of more than 1000 h for PEC water splitting at a low potential of 0.4 V vs. RHE using vigorous Mo-doped BiVO_4 photoanode. The photocorrosion was decreased by improving the intrinsic stability of Mo-doped BiVO_4 photo anode via high temperature treatment. Fe-incorporated Ni-based OEC by in-situ regeneration also played important role to attain the excellent stability, which can be of great use in increasing the photo stability of other photo electrodes for PEC water splitting. In addition to the modification of photoelectrode itself, the stability can also be enhanced by modifying the electrolyte composition.

The dissolution of V^{5+} from the BiVO_4 lattice is accountable for anodic photo corrosion of BiVO_4 . The use of V^{5+} saturated electrolyte was verified to be an effective method to suppress the anodic photocorrosion of BiVO_4 photoanode and stability of approximately 500 hours has been achieved by $\text{BiVO}_4/\text{FeOOH}/\text{NiOOH}$ photoanode through changing the electrolyte composition. Wang et al. [81] also applied electrolyte composition change by adding Fe^{2+} ions (0.1 M FeSO_4) in 1 M borate buffer electrolyte to suppress instability of plasma-etched $\text{NiOOH}/\text{BiVO}_4$ photoanode, primary to a notable oxygen evolution for >200 h. Other Bi-based photoelectrodes such as Bi_2WO_6 , Bi_2MoO_6 , BiOI , BiOCl and BiOBr are still coming out for the application of PEC water splitting. Much

effort are required to improve their PEC performance and later their stability without compromising the performance.

- [1] T. Minakata, K. Kubota, K. Domen, *Chem. Soc. Rev.* 43 (2014) 7110–7124.
- [2] D. Liu, X.K. Saltsman, D. Hong, P. Yang, *Angew. Chem. Int. Ed.* 54 (2015) 1259–1266.
- [3] A. Fujishima, K. Honda, *Nature* 238 (1972) 37–38.
- [4–11] Jun, W., Hai-Xia Z., Zhong-Li W., Fan-Li M., Xin-Da Z. Integrated three-dimensional carbon-polyacetylene tubes/cobalt-nitride sheets as an efficient electrode for overall water splitting. *ACS Nano* 2016;10:1742–48.
- [5] Zhang Y., Luo K., Mo Y., Shi X., Oshiki T., Morishita K. Plasmon-assisted water splitting using two sides of the same SrTiO₃ single-crystal substrate: conversion of visible light to chemical energy. *Angew. Chemie Int. Ed.* 2014;53:10350–1.
- [6] Sathish M, Viswanathan B, Viswanath RP. Atomless synthetic strategy for the preparation of CuS nanoparticles and its exploitation for water splitting. *Int J Hydrogen Energy* 2006;31:1891–98.
- [7] A. Waleed, W.A. Smith, T.R. Kuykendall, Y. Zhao, J.Z. Zhang, *Adv. Funct. Mater.* 18 (2009) 1849–1858.
- [8] Szymanski P, El-Sayed MA. Some recent developments in photoelectrochemical water splitting using nanostructured TiO₂ a short review. *Thin Film Adv.* 2012;13:1–20.
- [9] Z. Zhang, C. Gao, Z. Wu, W. Han, Y. Wang, W. Fu, X. Li, L. Xu, *Photo-Chem* 10 (2020) 318–322.
- [10] M. Pease, N.T. Nolan, K.C. Pillay, M.R. Gory, P. Tamar, A.G. Kottur, P. J. Doolan, J.W. Hurren, J.A. Byrne, K. O'Shea, *Appl. Catal. B* 125 (2012) 33–43.
- [11] Y. Wang, W. Tian, G. Chen, W. Xu, L. Li, *Adv. Funct. Mater.* 29 (2019) 180236.
- [12] T. Zhu, M.N. Cheng, L.S. Chen, *ChemSusChem* 7 (2014) 2074–2077.
- [13] L. Wang, N.T. Nguyen, X. Huang, P. Schirek, Y. Bi, *Adv. Funct. Mater.* 27(2017) 1703521.
- [14] J. Wang, S. Pan, M. Chen, D.A. Dixon, *J. Phys. Chem. C* 117 (2013) 22061–22068.
- [15] H. Ji, S. Shao, G. Yuan, C. Lu, K. Jing, Y. Xia, X. Li, J. Zhang, H. Xu, J. Gong, *J. Energy Chem.* 52 (2020) 147–154.
- [16] S.S. Hhar, H.W. Jang, *Catalysis Chem* 10 (2017) 3001–3018.
- [17] S. Ramalingam, T.G. Lee, C. Yang, *Nano Lett.* 14 (2014) 4517–4522.
- [18] J.H. Kim, I.S. Lee, *Adv. Mater.* 31 (2019) 1808934.
- [19] C.S. Yano, M.N. Cheng, A.K. Soti, *Adv. Sci. Tech.* 30 (2017) 9–16.
- [20] Y. Park, K.J. McDonnell, K.-S. Choi, *Chem. Soc. Rev.* 42 (2013) 2321–2337.

- [1] T.-F. Hou, M.A. Johar, R. Boppella, M.A. Hassan, S.J. Patil, S.-W. Ryu, D.-W. Lee, *J. Energy Chem.* 49 (2020) 262–274.
- [2] T. Hisatomi, J. Kubota, K. Domen, *Chem. Soc. Rev.* 43 (2014) 7520–7535.
- [3] D. Kim, K.K. Sakimoto, D. Hong, P. Yang, *Angew. Chem. Int. Ed.* 54 (2015) 3259–3266.
- [4] A. Fujishima, K. Honda, *Nature* 238 (1972) 37–38.
- [4-1] Jun W, Hai-Xia Z, Zhong-Li W, Fan-Lu M, Xin-Bo Z. Integrated three-dimensional carbon paper/carbon tubes/ cobalt-sulfide sheets as an efficient electrode for overall water splitting. *ACS Nano* 2016;10:2342e8
- [5] Zhong Y, Ueno K, Mori Y, Shi X, Oshikiri T, Murakoshi K. Plasmon-assisted water splitting using two sides of the same SrTiO₃ single-crystal substrate: conversion of visible light to chemical energy. *AngewChemie Int Ed* 2014;53:10350e4.
- [6] Sathish M, Viswanathan B, Viswanath RP. Alternate synthetic strategy for the preparation of CdS nanoparticles and its exploitation for water splitting. *Int J Hydrogen Energy* 2006;31:891e8.
- [7] A. Wolcott, W.A. Smith, T.R. Kuykendall, Y. Zhao, J.Z. Zhang, *Adv. Funct. Mater.* 19 (2009) 1849–1856.
- [8] Szymanski P, El-Sayed MA. Some recent developments in photoelectrochemical water splitting using nanostructured TiO₂: a short review. *Theor Chem Acc* 2012;131:1202.
- [9] Z. Zhang, C. Gao, Z. Wu, W. Han, Y. Wang, W. Fu, X. Li, E. Xie, *Nano Energy* 19(2016) 318–327.
- [10] M. Pelaez, N.T. Nolan, S.C. Pillai, M.K. Seery, P. Falaras, A.G. Kontos, P.S. Dunlop, J.W. Hamilton, J.A. Byrne, K. O'shea, *Appl. Catal. B* 125 (2012) 331–349.
- [11] Y. Wang, W. Tian, C. Chen, W. Xu, L. Li, *Adv. Funct. Mater.* 29 (2019) 1809036.
- [12] T. Zhu, M.N. Chong, E.S. Chan, *ChemSusChem* 7 (2014) 2974–2997.
- [13] L. Wang, N.T. Nguyen, X. Huang, P. Schmuki, Y. Bi, *Adv. Funct. Mater.* 27(2017) 1703527.
- [14] J. Wang, S. Pan, M. Chen, D.A. Dixon, *J. Phys. Chem. C* 117 (2013) 22060–22068.
- [15] H. Ji, S. Shao, G. Yuan, C. Lu, K. Feng, Y. Xia, X. Lv, J. Zhong, H. Xu, J. Deng, *J. Energy Chem.* 52 (2020) 147–154.
- [16] S.S. Bhat, H.W. Jang, *ChemSusChem* 10 (2017) 3001–3018.
- [17] S. Ramadurgam, T.G. Lin, C. Yang, *Nano Lett.* 14 (2014) 4517–4522.
- [18] J.H. Kim, J.S. Lee, *Adv. Mater.* 31 (2019) 1806938.
- [19] C.S. Yaw, M.N. Chong, A.K. Soh, *Adv. Sci. Tech.* 99 (2017) 9–16.
- [20] Y. Park, K.J. McDonald, K.-S. Choi, *Chem. Soc. Rev.* 42 (2013) 2321–2337.

- [21] L. Han, F.F. Abdi, R. van de Krol, R. Liu, Z. Huang, H.J. Lewerenz, B. Dam, M.Zeman, A.H. Smets, *ChemSusChem* 7 (2014) 2832–2838.
- [22] P. Luan, J. Zhang, *ChemElectroChem* 6 (2019) 3227–3243.
- [23] W. Zhang, L. Song, J. Cen, M. Liu, *J. Phys. Chem. C* 123 (2019) 20730–20736.
- [24] S.A. Monny, L. Zhang, Z. Wang, B. Luo, M. Konarova, A. Du, L. Wang, *J. Mater.Chem. A* 8 (2020) 2498–2504.
- [25] C. Zhang, Y. Li, M. Chu, N. Rong, P. Xiao, Y. Zhang, *RSC Adv.* 6 (2016) 24760–24767.
- [26] S.A. Monny, Z. Wang, T. Lin, P. Chen, B. Luo, L. Wang, *Chem. Commun.* 56(2020) 9376–9379.
- [27] S. Wang, P. Chen, J.H. Yun, Y. Hu, L. Wang, *Angew. Chem. Int. Ed.* 56 (2017)8500–8504.
- [28] S.Y. Chae, E.S. Lee, H. Jung, Y.J. Hwang, O.-S. Joo, *RSC Adv.* 4 (2014) 24032–24037.
- [29] C. Yu, Z. Wu, R. Liu, D.D. Dionysiou, K. Yang, C. Wang, H. Liu, *Appl. Catal. B* 209(2017) 1–11.
- [30] K.-H. Ye, Z. Chai, J. Gu, X. Yu, C. Zhao, Y. Zhang, W. Mai, *Nano Energy* 18 (2015)222–231.
- [31] C. Liu, J. Zhou, J. Su, L. Guo, *Appl. Catal. B* 241 (2019) 506–513.
- [32] Z.-Q. Wang, H. Wang, X.-F. Wu, T.-L. Chang, *J. Alloys Compd.* 834 (2020)155025.
- [33] S.P. Berglund, F.F. Abdi, P. Bogdanoff, A. Chemseddine, D. Friedrich, R. van de Krol, *Chem. Mater.* 28 (2016) 4231–4242.
- [34] F. Wang, W. Septina, A. Chemseddine, F.F. Abdi, D. Friedrich, P. Bogdanoff, R.van de Krol, S.D. Tilley, S.P. Berglund, *J. Am. Chem. Soc.* 139 (2017) 15094–15103.
- [35] L. Zhu, P. Basnet, S.R. Larson, L.P. Jones, J.Y. Howe, R.A. Tripp, Y. Zhao, *ChemistrySelect* 1 (2016) 1518–1524.
- [36] T. Arai, Y. Konishi, Y. Iwasaki, H. Sugihara, K. Sayama, *J. Comb. Chem.* 9 (2007) 574–581.
- [37] F. Wang, A. Chemseddine, F.F. Abdi, R. van de Krol, S.P. Berglund, *J. Mater.Chem. A* 5 (2017) 12838–12847.
- [38] K.-H. Ye, Z. Chai, J. Gu, X. Yu, C. Zhao, Y. Zhang, W. Mai, *Nano Energy* 18 (2015)222–231.
- [39] J. Yang, C. Du, Y. Wen, Z. Zhang, K. Cho, R. Chen, B. Shan, *Int. J. Hydrog. Energy*43 (2018) 9549–9557.
- [40] J. Li, M.H. Griep, Y. Choi, D. Chu, *Chem. Commun.* 54 (2018) 3331–3334.

- [41] M.G. Walter, E.L. Warren, J.R. McKone, S.W. Boettcher, Q. Mi, E.A. Santori, N.S. Lewis, *Chem. Rev.* 110 (2010) 6446–6473.
- [42] J. Wang, J. Neaton, H. Zheng, V. Nagarajan, S. Ogale, B. Liu, D. Viehland, V. Vaithyanathan, D. Schlom, U. Waghmare, *Science* 299 (2003) 1719–1722.
- [43] M. Tomczyk, D.G. Stroppa, I.M. Reaney, P.M. Vilarinho, *Phys. Chem. Chem. Phys.* 19 (2017) 14337–14344.
- [44] J. Gómez, C. Canaria, R.O. Burgos, C. Ortiz, G. Supelano, C.P. Vargas, *J. Phys. Conf. Series* 687 (2016) 1–4.
- [45] J.-M. Moreau, C. Michel, R. Gerson, W.J. James, *J. Phys. Chem. Solids* 32 (1971) 1315–1320.
- [46] X. Xu, Y.H. Lin, P. Li, L. Shu, C.W. Nan, *J. Am. Ceram. Soc.* 94 (2011) 2296–2299.
- [47] D. Cao, N. Nasori, Z. Wang, Y. Mi, L. Wen, Y. Yang, S. Qu, Z. Wang, Y. Lei, *J. Mater. Chem. A* 4 (2016) 8995–9001.
- [48] M. Murakami, S. Fujino, S.-H. Lim, L. Salamanca-Riba, M. Wuttig, I. Takeuchi, B. Varughese, H. Sugaya, T. Hasegawa, S. Lofland, *Appl. Phys. Lett.* 88 (2006) 112505.
- [49] S.J. Moniz, C.S. Blackman, P. Southern, P.M. Weaver, J. Tang, C.J. Carmalt, *Nanoscale* 7 (2015) 16343–16353.
- [50] W. Li, K. Jiang, Z. Li, S. Gong, R.L. Hoyer, Z. Hu, Y. Song, C. Tian, J. Kim, K.H. Zhang, *Adv. Energy Mater.* 8 (2018) 1801972.
- [51] S. Cho, J.-W. Jang, W. Zhang, A. Suwardi, H. Wang, D. Wang, J.L. MacManus-Driscoll, *Chem. Mater.* 27 (2015) 6635–6641.
- [52] D. Cao, Z. Wang, L. Wen, Y. Mi, Y. Lei, *Angew. Chem.* 126 (2014) 11207–11211.
- [53] J. Xie, C. Guo, P. Yang, X. Wang, D. Liu, C.M. Li, *Nano Energy* 31 (2017) 28–36.
- [54] W. Ji, K. Yao, Y.-F. Lim, Y.C. Liang, A. Suwardi, *Appl. Phys. Lett.* 103 (2013) 062901.
- [55] Q. Zhang, W. Gong, J. Wang, X. Ning, Z. Wang, X. Zhao, W. Ren, Z. Zhang, *J. Phys. Chem. C* 115 (2011) 25241–25246.
- [56] B. Li, C. Lai, G. Zeng, L. Qin, H. Yi, D. Huang, C. Zhou, X. Liu, M. Cheng, P. Xu, *ACS Appl. Mater. Interfaces* 10 (2018) 18824–18836.
- [57] Y. Wang, M. Daboczi, C.A. Mesa, S.R. Ratnasingham, J.-S. Kim, J.R. Durrant, S. Dunn, H. Yan, J. Briscoe, *J. Mater. Chem. A* 7 (2019) 9537–9541.
- [58] S.M. Selbach, T. Tybell, M.A. Einarsrud, T. Grande, *Adv. Mater.* 20 (2008) 3692–3696.
- [59] T.W. Kim, K.-S. Choi, *Science* 343 (2014) 990–994.
- [60] S. Wang, P. Chen, Y. Bai, J.H. Yun, G. Liu, L. Wang, *Adv. Mater.* 30 (2018) 1800486.

- [61] Y. Qiu, W. Liu, W. Chen, G. Zhou, P.-C. Hsu, R. Zhang, Z. Liang, S. Fan, Y. Zhang, Y. Cui, *Sci. Adv.* 2 (2016) e1501764.
- [62] T.W. Kim, Y. Ping, G.A. Galli, K.-S. Choi, *Nat. Commun.* 6 (2015) 1–10.
- [63] Y. Zhao, G. Brocks, H. Genuit, R. Lavrijsen, M.A. Verheijen, A. Bieberle-Hütter, *Adv. Energy Mater.* 9 (2019) 1900940.
- [64] M. Huang, J. Bian, W. Xiong, C. Huang, R. Zhang, *J. Mater. Chem. A* 6 (2018) 3602–3609.
- [65] D.K. Zhong, S. Choi, D.R. Gamelin, *J. Am. Chem. Soc.* 133 (2011) 18370–18377.
- [66] L. Wang, R. Wang, Y. Zhou, Q. Shen, J. Ye, C. Wu, Z. Zou, *Catal. Today* 335 (2019) 262–268.
- [67] Y. Pihosh, I. Turkevych, K. Mawatari, J. Uemura, Y. Kazoe, S. Kosar, K. Makita, T. Sugaya, T. Matsui, D. Fujita, *Sci. Rep.* 5 (2015) 11141.
- [68] Z. Tian, P. Zhang, P. Qin, D. Sun, S. Zhang, X. Guo, W. Zhao, D. Zhao, F. Huang, *Adv. Energy Mater.* 9 (2019) 1901287.
- [69] H.S. Han, S. Shin, D.H. Kim, I.J. Park, J.S. Kim, P.-S. Huang, J.-K. Lee, I.S. Cho, X. Zheng, *Energy Environ. Sci.* 11 (2018) 1299–1306.
- [70] K.-H. Ye, H. Li, D. Huang, S. Xiao, W. Qiu, M. Li, Y. Hu, W. Mai, H. Ji, S. Yang, *Nat. Commun.* 10 (2019) 1–9.
- [71] C. Wang, X. Ke, J. Wang, R. Liang, Z. Luo, Y. Tian, D. Yi, Q. Zhang, J. Wang, X.-F. Han, *Nat. Commun.* 7 (2016) 1–9.
- [72] N. Kim, R.-N. Vannier, C.P. Grey, *Chem. Mater.* 17 (2005) 1952–1958.
- [73] Z. Jiang, X. Liang, H. Zheng, Y. Liu, Z. Wang, P. Wang, X. Zhang, X. Qin, Y. Dai, M.-H. Whangbo, *Appl. Catal. B* 219 (2017) 209–215.
- [74] L. Liang, F. Lei, S. Gao, Y. Sun, X. Jiao, J. Wu, S. Qamar, Y. Xie, *Angew. Chem. Int. Ed.* 54 (2015) 13971–13974.
- [75] G. Dong, Y. Zhang, W. Wang, L. Wang, Y. Bi, *Energy Technol.* 5 (2017) 1912–1918.
- [76] R. Ullah, M. Pei, J. Wu, Y. Tian, Z. Gu, Q. Zhang, C. Song, Y. Yang, M. Ahmad, J. Zeb, *ACS Appl. Energy Mater.* 3 (2020) 4149–4154.
- [77] B. Moss, H. Le, S. Corby, K. Morita, S. Selim, C. Sotelo-Vazquez, Y. Chen, A. Borthwick, A. Wilson, C. Blackman, *J. Phys. Chem. C* 124 (2020) 18859–18867.
- [78] L. Zhang, C. Baumanis, L. Robben, T. Kandiel, D. Bahnemann, *Small* 7 (2011) 2714–2720.
- [79] S. Wei, N. Xu, F. Li, X. Long, Y. Hu, L. Gao, C. Wang, S. Li, J. Ma, J. Jin, *ChemElectroChem* 6 (2019) 3367–3374.

- [80] Y. Shimodaira, H. Kato, H. Kobayashi, A. Kudo, J. Phys. Chem. B 110 (2006) 17790–17797.
- [81] R.T. Gao, D. He, L. Wu, K. Hu, X. Liu, Y. Su, L. Wang, Angew. Chem. 132 (2020) 6272–6277.
- [82] M. Wu, Y. Wang, Y. Xu, J. Ming, M. Zhou, R. Xu, Q. Fu, Y. Lei, ACS Appl. Mater. Interfaces 9 (2017) 23647–23653.
- [83] Y. Ma, Y. Jia, L. Wang, M. Yang, Y. Bi, Y. Qi, Appl. Surf. Sci. 390 (2016) 399–405.

Chapter-III

Materials and Methods

The starting materials for the synthesis of BFO are bismuth nitrate pentahydrate, $\text{Bi}(\text{NO}_3)_3 \cdot 5\text{H}_2\text{O}$ and ferric nitrate nonahydrate $\text{Fe}(\text{NO}_3)_3 \cdot 9\text{H}_2\text{O}$ (all from Loba Chemie Pvt. Ltd), ethylene glycol (Thomas baer, Mumbai, India) were of analytical grade and used with no any further purification. Initially $\text{Bi}(\text{NO}_3)_3 \cdot 5\text{H}_2\text{O}$ was added in ethylene glycol in molar ratio of 1:1 with respect to ferric nitrates. The above solution was kept under constant magnetic stirring about a half an hour. Further ferric nitrate monohydrate was mixed into the above solution and heated at $\sim 90^\circ\text{C}$ under the stable magnetic stirring till all fluid gets evaporated out from the solution.

Subsequently, the produced brown powder was annealed in ambient temperature at heating rate of 5°C min^{-1} and kept at 600°C , for different time interval like 2 hr, 4 hr and 6 h to obtain well crystalline BFO nanoparticles. The synthesized BFO nanoparticles were examined by XRD model 600 Miniflex Rigaku to confirm the phase of the sample. The morphology of sample was examined by SEM model Nova Nano SEM-NPEP303.

3.1) Sol-Gel Method

Sol gel process steps:

i) Homogeneous solution

In the sol gel process we aim to produce homogeneous solution of precursors and alcohols. For doing this, first the solvent (usually containing water, alcohol and organic solvents) and the precursor are mixed in a container to obtain a homogeneous solution. To obtain a homogeneous solution, a mixture of two solvents with specific concentrations is often used to completely dissolve the precursors. For example, some organic metallic precursors first must be dissolved in water soluble organic solvent and then the resulting solution is dissolve in water. However in case of metal salt, it is soluble directly in water and does not require an organic solvent. In general alkoxide precursors are more widely used.

ii) Sol Formation

Once forming a homogeneous solution, it should be converted to tuberculosis. This phase is formed during the hydrolysis reaction. The term decomposition means that break down of complex compounds into simpler ones [1-3]. In general the reaction in which, the molecules are broken down into simpler molecules in presence of water is known as hydrolysis. Fig 1 below shows the flow chart of steps involved in the sol gel process.

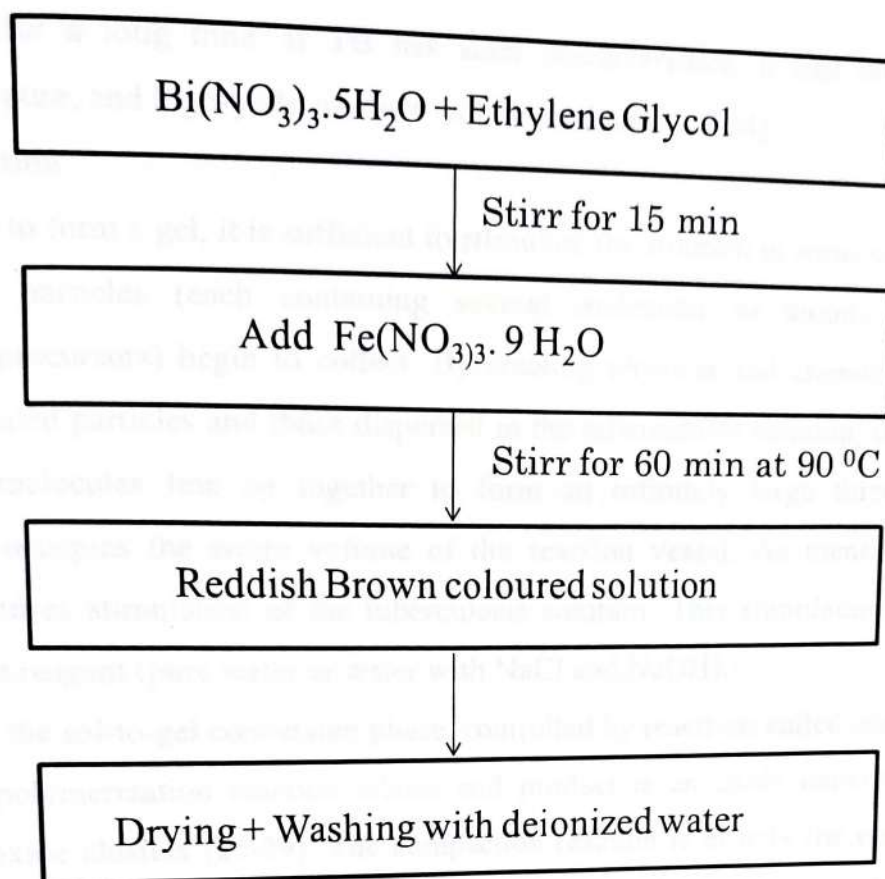


Fig 1: Flow chart of reaction method

This includes the formation of homogeneous solution, the formation of sol, the conversion of sol into gel and the removal of solvent from the gel (drying). Hydrolysis reaction is initiated by adding some water to the reaction medium. Due to hydrolysis reaction, the metal oxide particles come together and formed fine and solid particles dispersed in the solvent [4-9]. In a real solution, the solute is dispersed uniformly in the solvent as an atom, molecule, or ion, and the particle size does not exceed 1 nm. If the particle size of the solvent is greater than 100 nm, the particles gradually settle to form a suspension mixture [10-14]. If the particle size varies between 1 and 100 nanometers, they usually remain scattered throughout the mixture, which is called colloid.

Sol consists of very fine particles (less than 100 nm) dispersed in the solvent phase and are, in fact, a solution or more precisely a colloidal mixture [15-18]. Thus, according to the above explanations, a comprehensive definition of tuberculosis can be given; the most important thing to say about a good quality TB is that the resulting TB must be prepared in such a way that it can be stable for months and not settled. In other words, the particle size must be small enough that the Brownian motion of the particles overcomes the force of gravity and prevents them from settling. In this way, the resulting mixture remains

homogeneous for a long time. If TB has such characteristics, it can be hoped that a homogeneous, pure, and high-yield product will be produced [19-24].

iii) Gel Formation

In order to form a gel, it is sufficient to stimulate the solution in some way, so that the dispersed fine particles (each containing several molecular or atomic units of the corresponding precursors) begin to collect. By creating physical and chemical interactions between suspended particles and those dispersed in the tuberculosis solution, units of tens of thousands of molecules line up together to form an infinitely large three-dimensional molecule that occupies the entire volume of the reaction vessel. As mentioned, wet gel production requires stimulation of the tuberculosis solution. This stimulation can be done using a suitable reagent (pure water or water with NaCl and NaOH).

In fact, the sol-to-gel conversion phase, controlled by reactions called condensation, is an inorganic polymerization reaction whose end product is an oxide network containing MOM metal oxide clusters [25-29]. The compaction reaction is exactly the opposite of the hydrolysis reaction. In the hydrolysis reaction, large molecules are converted into simpler components by consuming water, but in the compaction reaction two simple molecules combine to form a more complex molecule. As the molecules combine in the compaction reaction, a small molecule such as water is released. A compaction reaction is possible when two hydroxides (or one hydroxide + one metal alkoxide) ($M-OR + HO-M$) combine to form a metal oxide ($MO-M$) [30-33].

Therefore, the gel produced will be soluble and in order to complete the sol-gel process and achieve a dry gel, the solvent must be separated using some methods. Produced gels have different types depending on the solvent used or the drying method and show various properties and applications [34,35].

Application of the Nanomaterials Prepared by Sol-Gel Method

- (i) Synthesis at low temperature
- (ii) Preparation of high purity products
- (iii) Very high production efficiency
- (iv) Production of optical components with complex shapes.

3.2) Characterization Techniques

3.2.1) X-ray diffraction technique

XRD is one of the most primary and widely used techniques to determine the crystal structure of the material. When a beam of X-rays interacts with atoms within the material it gets diffracted. The diffraction takes place in certain specific direction exactly similar as that

of light diffracted from grating. The diffraction pattern of such beam of electron can help us to determine crystal structure of the material.

Max von Laue, in 1912, discovered that crystalline substances act as the diffraction gratings for X-rays since the wavelength of incident X-rays is comparable with interplaner spacing in crystalline material. X-rays have wavelengths of the order of few angstroms same as that of inter planer spacing in crystalline solids so that they can interact with atoms and get the information at atomic level. When a beam of X-rays interact with atoms it produces constructive as well as destructive interferences which depend on the path difference between an incident and diffracted beam of X-rays. These patterns can be used as 'fingerprints' for the identification of solid phase. Fig 2 shows components of the X-ray diffraction system. The X-ray diffractometer mainly consists of four components a X-ray tube (source) for producing X-rays, the sample holder to hold the sample, an X-ray detector for detecting diffracted X-rays and Goniometer.

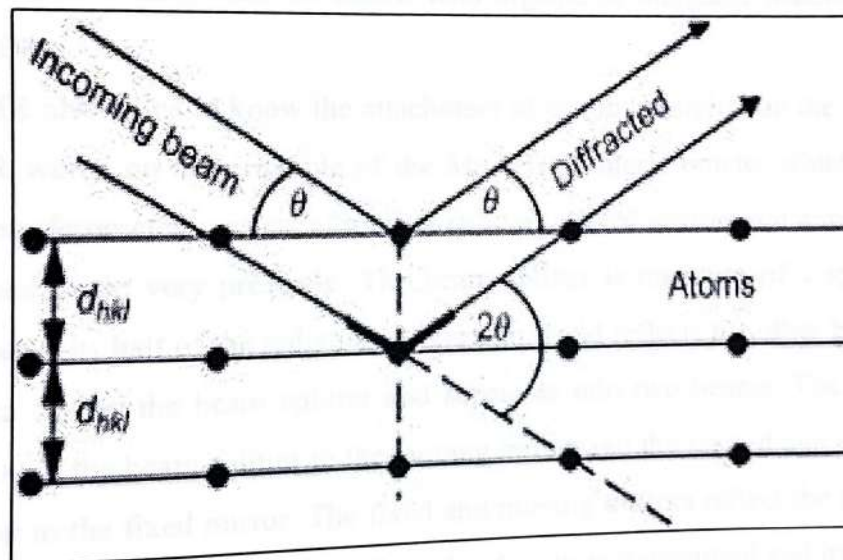


Fig 2: Schematic diagram of X-ray diffraction system.

When a monochromatic beam of X-ray is incident on crystalline material part of it is diffracted. The diffracted X-rays gives rise to constructive as well as destructive interference. The destructive interference occurs when the waves are out of phase. Those atoms which are arranged in crystal are regular and periodic gives constructive interference.

So that

$$2d \sin \theta = n \lambda \dots\dots\dots 1$$

Bragg reflection can occur only when $\lambda \sim d$; so cannot be used for visible light. The diffracted intensities are plotted against the detector angle 2θ . Bragg's law states the condition for sharp diffraction peak from the crystal. As crystallite dimension is reduced and

enter in the nanoscale the peaks get broaden. To determine the crystallite size, width of the diffraction peak can be use and this can be determined by using Scherer's formula

$$t = \frac{k \cdot \lambda}{\beta \cos \theta} \dots \dots \dots 2$$

Where, "t" is thickness of the crystal, k is a constant which depends on crystallite shape, for spherical particle, $k \sim 0.9$ and β is the full width at half maximum (FWHM) of highest intensity peak.

3.2.2) Fourier Transform Infra Red Spectroscopy

Fourier Transform Infrared (FTIR) spectroscopy is a method used for characterizing the organic and inorganic compounds. The FTIR spectrum provides the information about the presence of functional groups close to molecular structures. In most of the compounds it can also be used for confirmation of the phase on the basis of molecular vibrations. For example, in ferrites, the phase confirmation was done on the basis of presence or absence of octahedral and tetrahedral molecular vibrations. For the probable use of magnetic nanoparticles in biomedical applications they must be coated with organic or inorganic materials which are also biocompatible.

3.2.3) The FTIR also helps to know the attachment of coating material on the surface of the core. The FTIR works on the principle of the Michelson interferometer which is shown in figure 3. The interferometer consists of a beam splitter, a fixed mirror, and a mirror which is moving back and forth, very precisely. The beam splitter is made up of a special type of material that transmits half of the radiation striking on it and reflects the other half. Radiation from the source strikes the beam splitter and separates into two beams. The first beam is transmitted through the beam splitter to the moving mirror and the second one is reflected off the beam splitter to the fixed mirror. The fixed and moving mirrors reflect the radiation back to the beam splitter. Again, half of this reflected radiation is transmitted and half is reflected at the beam splitter, resulting in one beam passing to the detector and the second back to the source.

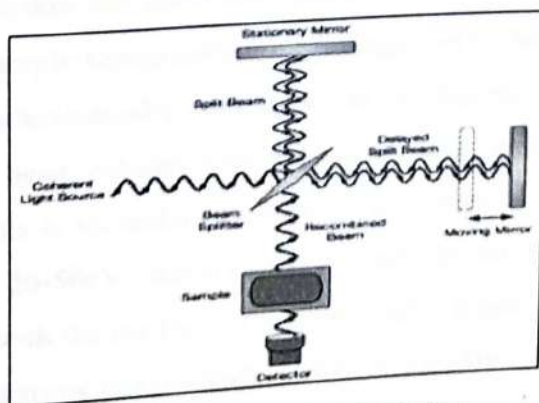


Fig 3: FTIR Spectrometer

The working on the infrared technique is based on a simple fact; on incidence of infrared radiation proportion of it is absorbed and transmits at each frequencies or wavelengths. We define I_0 to be the intensity of the light incident upon the sample and I to be the intensity of the beam after it interacted with the sample.

The aim of the basic infrared experiment is to determine the intensity ratio I/I_0 as a function of the frequency (w) or wave number which is the reciprocal of wavelength of the light. A plot of this ratio versus the wave number is nothing but the infrared spectrum. The infrared spectrum is commonly plotted in one of three formats: as transmittance, absorbance, or reflectance. If one can measure the fraction of light transmitted through the sample, this ratio is defined as

$$T = \frac{I_t}{I_0} \dots \dots \dots 3$$

Where T , is the transmittance of the sample, and I_t is the intensity of the transmitted light. Similarly, if one is measuring the light reflected from the surface of the sample, then the ratio is equated to R_w or the reflectance of the spectrum, with I_t being replaced with the intensity of the reflected light I_r .

3.2.3) Electron Microscopy

As reducing the size of a material under investigation it is very difficult to resolve the physical parameters so as to make a need of advanced characterization of materials with spatial resolution, to obtain deep understanding of the materials structure. To triumph over this difficulty an electron microscope plays a key tool to characterize the material to obtain information like morphology, topography, composition of a wide range of materials. An electron microscopy is a technique which uses electrons as a source of illumination and produces images when interacts with the sample. Before going to the scanning and transmission electron microscopy first understand the different interaction mechanisms which take place on the incidence of electron beam on the surface of the sample. When the higher energy electron beam strikes the specimen, produces various signals. These signals contain information about the sample topography, morphology, crystallographic arrangement etc.

The Fig.4 shows schematically various kinds of signals takes place after interaction. When incident electron beam collides with the sample atom in elastically, electron is emitted from one of the shell this is secondary electron. The energy of these electrons is very weak and it lies between 20-50eV. Backscattered electrons are produced when high energy electron beam collides with the nucleus of a sample atom it gets reflect off the sample atoms. The energy of these electrons is very high since it collides elastically with sample atoms. Due to transition of electrons from their inner shell the characteristic X-rays are produced.

The Auger electrons are also produced from top of the surface. The emitted electrons can be detected by using various detectors.

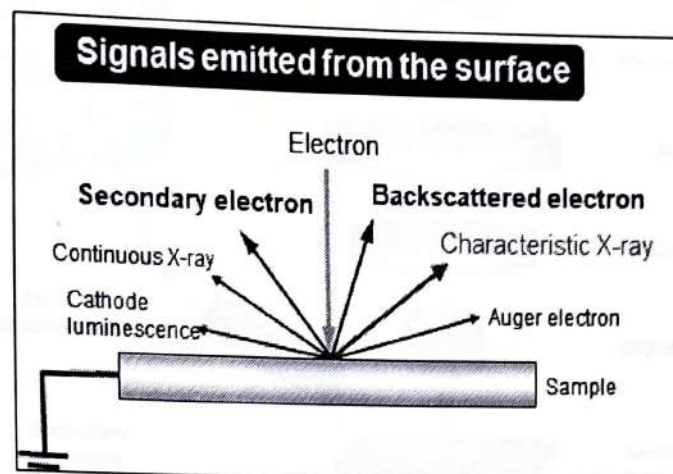


Fig 4: Intraction of electron with the sample

1) Scanning Electron Microscopy(SEM)

Scanning electron microscope is a type of electron microscopy that can be used to images a sample by scanning it with a high energy beam of electrons in a raster scan pattern. The beam of electrons interact with atoms of the sample and producing signals which contain information about the surface morphology of the sample, composition and other properties . Characteristics that can be viewed on SEM:

- 1) Topography: It is associated to the surface features of an object or “how it looks”, its texture.
 - 2) Morphology: Basically morphology refers to the external appearance of the sample like shape and size of the particles that making up the sample.
 - 3) Composition: It is associated to the elements and compounds that the object is composed of and their relative concentration.
 - 4) Crystallographic arrangement: It provides the information about how the atoms are arranged inside the sample.
- Construction of SEM is shown in fig 5 below. The major parts of the SEM are as follows

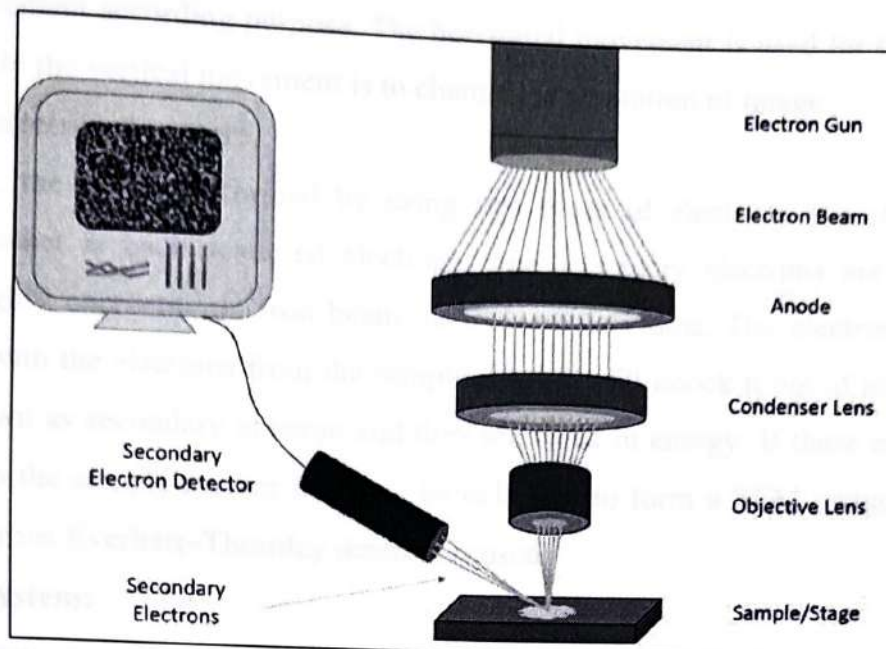


Fig 5: Scanning electron microscope

i) Electron Gun:

It can be used for the production of electron beam. In SEM mostly thermionic emission gun (TEG) is used. The electrons are emitted by means of thermionic emission from a filament (cathode) which is made up of a thin tungsten wire (about 0.1mm) by heating at high temperature. The ejected electrons are gathered as an electron beam which flows into the metal plate i.e anode by applying a positive voltage. Sometimes special type of electrode known as Wehnelt electrode is placed between cathode and anode. By applying a negative potential to this electrode, the speed of electron can be adjusted.

ii) Condenser Lens/electromagnetic Lens:

For obtaining a quality image an electron beam should be very fine. This can be obtained by placing a lens below the electron gun which enables to adjust the diameter of the electron beam. The role of condenser lens is formation of fine electron beam.

iii) Objective lens:

To obtain a good image the focusing of the electron beam to a particular spot is so important and this can be achieved with the help of objective lens. Scanning coils: Scanning coils are the sets of plates around the electron beam. Deflection of electron beam takes place by varying the potential between them. If the plates are attached to a scan generator, the beam is able to scan lines across the sample.

iv) Specimen stage:

The specimen stage supports the sample. It can perform horizontal (X,Yaxis) and vertical movements (Z-axis) so that tilting and rotation of the specimen occurs. We can use

any of the movement according purpose. The horizontal movement is used for the selection of the field while the vertical movement is to change the resolution of image.

v) Secondary electron detector:

In SEM, the image is formed by using two types of electrons one is secondary electrons and other is back scattered electrons. The secondary electrons are formed by striking the highly energetic electron beam on the sample atoms. The electrons from the beam collides with the electrons from the sample atom, it will knock it out of its shell. This electron is known as secondary electron and they are weak in energy. If these electrons are close enough to the sample surface they can be collected to form a SEM image. To detect secondary electrons Everhart–Thornley detector is used.

v) Operating system:

The output signals from secondary electron detector are amplified and then transferred to the display unit. Scanning on the display unit is synchronized with the help of electron probe scan that depends on the number of secondary electrons which appears on the monitor screen on the display unit thus forming a SEM image. The electron optical system and specimen chamber must be kept at a high vacuum of 10^{-3} - 10^{-4} Pa.

3.2.4) Photo activity and degradation mechanism of BiFeO₃

Since 2007, BFO has been largely studied due to its outstanding photoactivity. Up to the present time, it showed remarkable photo activity for the typical organic pollutants degradation. For aqueous media reactions, numerous organic pollutants such as methylene blue (MB), rhodamine B (RhB), methyl orange (MO), have been utilized as model contaminants. Nevertheless, there is a limited report in the literature for gaseous phase reactions. In those photocatalytic processes, frequent experimental factors were partook including nanostructure, surface area and loading of photocatalyst, kinds of organic pollutant, initial pollutant concentration and light source. Hence, a direct comparison of the photocatalytic experiments from laboratory to laboratory is difficult.

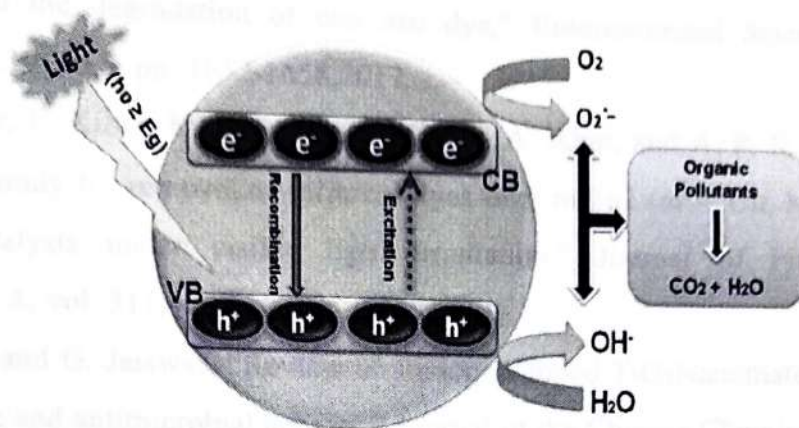
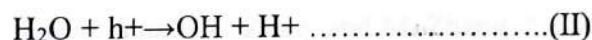
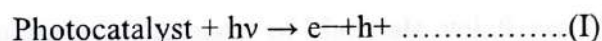
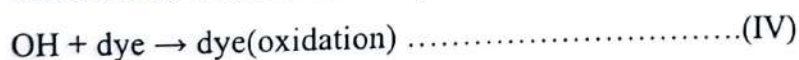


Fig 6: Basic mechanism of photocatalysis

The mechanism of photocatalysis is described in Eqs. (I–V), when the incoming light strike on target semiconductor (having energy greater or equal to band-gap), then electron and hole pair is created and they travel towards the photocatalyst's surface and redox reactions take place with the compounds that are bound on the surface of catalyst [35,36]. The water molecules get oxidized by the holes from valence band to produce hydroxyl radicals and then generated electrons in the conduction band reduced the dissolved oxygen in water to produce O_2^- .



The hydroxyl and O_2^- ions cause the redox reactions of the dye molecules and create smaller compounds and this causes dye de-colorization. The superoxide anion radicals are reproduced which reacts with H^+ ions and produce more OH^\cdot radicals [37].



- [1] Y.H. Shih and C.H. Lin, "Effect of particle size of Titanium dioxide nanoparticles aggregates on the degradation of one azo dye," *Environmental Science and Pollution Research*, vol. 19, no. 5, pp. 1652-1658, 2012.
- [2] O. Kerkez, E. Kibar, K. Dayioglu, F. Gedik, A. Akin, and A. P. S. O. Aydinoglu, "A comparative study for removal of different dyes over m/tio₂ (m = Cu, Ni, Co, Fe, Mn and Cr) photocatalysts under visible light irradiation," *Journal of Photochemistry and Photobiology A*, vol. 311, pp. 176-185, 2015.
- [3] S. Yadav and G. Jaiswar, "Review on undoped/doped TiO₂ Nanomaterial; synthesis and photocatalytic and antimicrobial activity," *Journal of the Chinese Chemical Society*, vol. 64, no. 1, pp. 103-116, 2017.
- [4] P. Peerakiatkhajohn, W. Onreabroy, C. Chawengkijwanich, and S. Chiarakorn, "Preparation of visible-light-responsive TiO₂ doped Ag thin film on PET plastic for BTEX treatment," *D-J Series Sustain. Energy Environ.* vol. 2, pp. 121-125, 2011.
- [5] H. Pan, X. D. Wang, S. S. Xiao, L. G. Yu, and Z. J. Zhang, "Preparation and characterization of TiO₂ nanoparticles surface-modified by octadecyltrimethoxysilane," *Indian Journal of Engineering and Materials Sciences*, vol. 20, no. 6, pp. 561-567, 2013.
- [6] B. B. Lakshmi, P. K. Dorhout, and C. R. Martin, "Sol-Gel template synthesis of semiconductor nanostructures," *Chemistry of Materials*, vol. 9, no. 3, pp. 857-862, 1997.
- [7] Z. Wang, L. Shi, F. Wu, S. Yuan, Y. Zhao, and M. Zhang, "The sol-gel template synthesis of porous TiO₂ for a high performance humidity sensor," *Nanotechnology*, vol. 22, no. 27, Article ID 275502, 2011.
- [8] X. Hou, M. Huang, X. Wu, and A. Liu, "Preparation and studies of photocatalytic silver-loaded TiO₂ films by hybrid sol-gel method," *Chemical Engineering Journal*, vol. 146, no. 1, pp. 42-48, 2009.
- [9] R.S. Dubey, "Temperature-dependent phase transformation of TiO₂ nanoparticles synthesized by sol-gel method," *Materials Letters*, vol. 215, pp. 312-317, 2018.
- [10] A. O. Araoyinbo, M. M. A. B. Abdullah, M. A. A. M. Salleh, N. N. A. Aziz, and A. A. Iskandar, "Phase study of titanium dioxide nanoparticle prepared via sol-gel process," *IOP Conference Series: Materials Science and Engineering*, vol. 343, Article ID 012011, 2018.
- [11] T. H. Mahato, G. K. Prasad, B. Singh, J. Acharya, A. R. Srivastava, and R. Vijayaraghavan, "Nanocrystalline zinc oxide for the decontamination of sarin," *Journal of Hazardous Materials*, vol. 165, no. 1-3, pp. 928-932, 2009.
- [12] C. Hariharan, "Photocatalytic degradation of organic contaminants in water by ZnO nanoparticles: Revisited," *Applied Catalysis A: General*, vol. 304, pp. 55-61, 2006.

- [13] M. Ristic, S. Musić, M. Ivanda, and S. Popovic, "Sol-gel synthesis and characterization of nanocrystalline ZnO powders," *Journal of Alloys and Compounds*, vol. 397, no. 1-2, 2005.
- [14] S. Yue, Z. Yan, Y. Shi, and G. Ran, "Synthesis of zinc oxide nanotubes within ultrathin anodic aluminum oxide membrane by sol-gel method," *Materials Letters*, vol. 98, pp. 246–249, 2013.
- [15] V. Mayekar, S. Dhar, and Radha, "To study the role of temperature and sodium hydroxide concentration in the synthesis of zinc oxide nanoparticles," *J. Sci. Res. Publ.* vol. 3, no. 11, pp. 2250–3153, 2013.
- [16] S. Zavar, "A novel three component synthesis of 2-amino-4H-chromenes derivatives using nano ZnO catalyst," *Arabian Journal of Chemistry*, vol. 10, pp. S67–S70, 2017.
- [17] N. K. Hassan, M. R. Hashim, and M. Bououdina, "Onedimensional ZnO nanostructure growth prepared by thermal evaporation on different substrates: ultraviolet emission as a function of size and dimensionality," *Ceramics International*, vol. 39, no. 7, pp. 7439–7444, 2013.
- [18] D. Ju, H. Xu, J. Zhang, J. Guo, and B. Cao, "Direct hydrothermal growth of ZnO nanosheets on electrode for ethanol sensing," *Sensors and Actuators B: Chemical*, vol. 201, pp. 444–451, 2014.
- [19] S. Yue, J. Lu, and J. Zhang, "Synthesis of three-dimensional ZnO superstructures by a one-pot solution process," *Materials Chemistry and Physics*, vol. 117, no. 1, pp. 4–8, 2009.
- [20] A. Sagasti, N. Bouropoulos, D. Kouzoudis, A. Panagiotopoulos, E. Topoglidis, and J. Gutierrez, "Nanostructured ZnO in a metglas/ZnO/hemoglobin modified electrode to detect the oxidation of the hemoglobin simultaneously by cyclic voltammetry and magnetoelastic resonance," *Materials*, vol. 10, no. 8, 2017.
- [21] P. Samanta, A. Saha, and T. Kamilya, "Chemical synthesis and optical properties of ZnO nanoparticles," *Journal of Nano- and Electronic Physics*, vol. 6, no. 4, pp. 04015-1–04015-2, 2014.
- [22] Y. Zhang and E. Xie, "Nature of room-temperature ferromagnetism from undoped ZnO nanoparticles," *Applied Physics A*, vol. 99, no. 4, pp. 955–960, 2010.
- [23] M. Navaneethan, G. K. Mani, S. Ponnusamy et al., "Influence of Al doping on the structural, morphological, optical, and gas sensing properties of ZnO nanorods," *Journal of Alloys and Compounds*, vol. 698, pp. 555–564, 2017.
- [24] J. T. Chen, J. Wang, R. F. Zhuo et al., "The effect of Al doping on the morphology and optical property of ZnO nanostructures prepared by hydrothermal process," *Applied Surface*

- Science, vol. 255, no. 7, pp. 3959–3964, 2009.
- [25] J. Wang, Y. Li, Y. Kong et al., "Non-fluorinated superhydrophobic and micro/nano hierarchical Al doped ZnO film: the effect of Al doping on morphological and hydrophobic properties," RSC Advances, vol. 5, no. 99, Article ID 81029, 2015.
- [26] S. S. Shinde, P. S. Shinde, Y. W. Oh, D. Haranath, C. H. Bhosale, and K. Y. Rajpure, "Structural, optoelectronic, luminescence and thermal properties of Ga-doped zinc oxide thin films," Applied Surface Science, vol. 258, no. 24, pp. 9969–9976, 2012.
- [27] S. K. Patil, S. S. Shinde, and K. Y. Rajpure, "Physical properties of spray deposited Ni-doped zinc oxide thin films," Ceramics International, vol. 39, no. 4, pp. 3901–3907, 2013.
- [28] S. S. Shinde, A. P. Korade, C. H. Bhosale, and K. Y. Rajpure, "Influence of tin doping onto structural, morphological, optoelectronic and impedance properties of sprayed ZnO thin films," Journal of Alloys and Compounds, vol. 551, pp. 688–693, 2013.
- [29] S. S. Shinde, P. S. Patil, R. S. Gaikwad, R. S. Mane, B. N. Pawar, and K. Y. Rajpure, "Influences in high quality zinc oxide films and their photoelectrochemical performance," Journal of Alloys and Compounds, vol. 503, no. 2, pp. 416–421, 2010.
- [30] S. S. Shinde and K. Y. Rajpure, "Fast response ultraviolet GadopedZnO based photoconductive detector," Materials Research Bulletin, vol. 46, no. 10, pp. 1734–1737, 2011.
- [31] R. Ullah and J. Dutta, "Photocatalytic degradation of organic dyes with manganese-doped ZnO nanoparticles," Journal of Hazardous Materials, vol. 156, no. 1-3, pp. 194–200, 2008.
- [33] M. K. Hossain, S. C. Ghosh, Y. Boontongkong, C. .anachayanont, and J. Dutta, "Growth of zinc oxide nanowires and nanobelts for gas sensing applications," Journal of Metastable and Nanocrystalline Materials, vol. 23, pp. 27–30, 2005vol. 120, pp. 1–9, 2013.
- [34] Y. Natsume and H. Sakata, "Zinc oxide films prepared by solgel spin-coating," 4in Solid Films, vol. 372, no. 1-2, pp. 30–36, 2000.
- [35] T. Nagase, T. Ooie, and J. Sakakibara, "A novel approach to prepare zinc oxide films: excimer laser irradiation of sol-gel derived precursor films," 4in Solid Films, vol. 357, no. 2, pp. 151–158, 1999
- [36] Kdasi A, Idris A, Saeed A, Guan K, Teong C. Treatment oftextile waste-water by advanced oxidation Processes-Areview. Global Nest: the Int. J 2004;60:222.
- [37] Elmolla, Emad S, Chaudhuri M. Comparison of differentadvanced oxidation processes for treatment of antibioticaqueous solution. Desalination 2010;256:43.
- [38] Rauf MA, Meetani MA, Hisaindee S. An overview on the photo catalytic degradation of azo dyes in the presence of TiO₂ doped with selective transition metals.

Chapter-IV

Results and Discussion

1. Structural Analysis

1.1) X-ray Diffraction Technique (XRD)

The XRD pattern of as synthesized BFO nanoparticles annealed for 2 hr, 4 hr, and 6 hr for 600 °C is shown in Fig 1, It is observed that all the diffraction peaks of the sample shows the expected peaks along with some impurity peaks emerging from the BFO rhombohedral structure having R3m space group (JCPDS No 74-2016). The lattice parameters of BFO nanoparticles were also determined and which are $a = b = 3.962 \text{ \AA}$. It is well-known that other phases including Bi_2O_3 , $\text{Bi}_2\text{Fe}_4\text{O}_9$, $\text{Bi}_{25}\text{FeO}_{40}$ and $\text{Bi}_{36}\text{Fe}_{24}\text{O}_{57}$ are repeatedly obtained during synthesis of BiFeO_3 especially in the bulk form [1].

The peaks representing BiFeO_3 are found in all the samples. However, as the annealing time is increased to 6 hr, the strong peaks characteristic of BiFeO_3 are obtained and the peak observed at $2\theta \cong 22^\circ$ due to the presence of secondary phase is reduced substantially. However, the intensity of the diffraction peaks of BFO samples becomes sharper and the impurity peaks gets reduced with increasing annealing time.

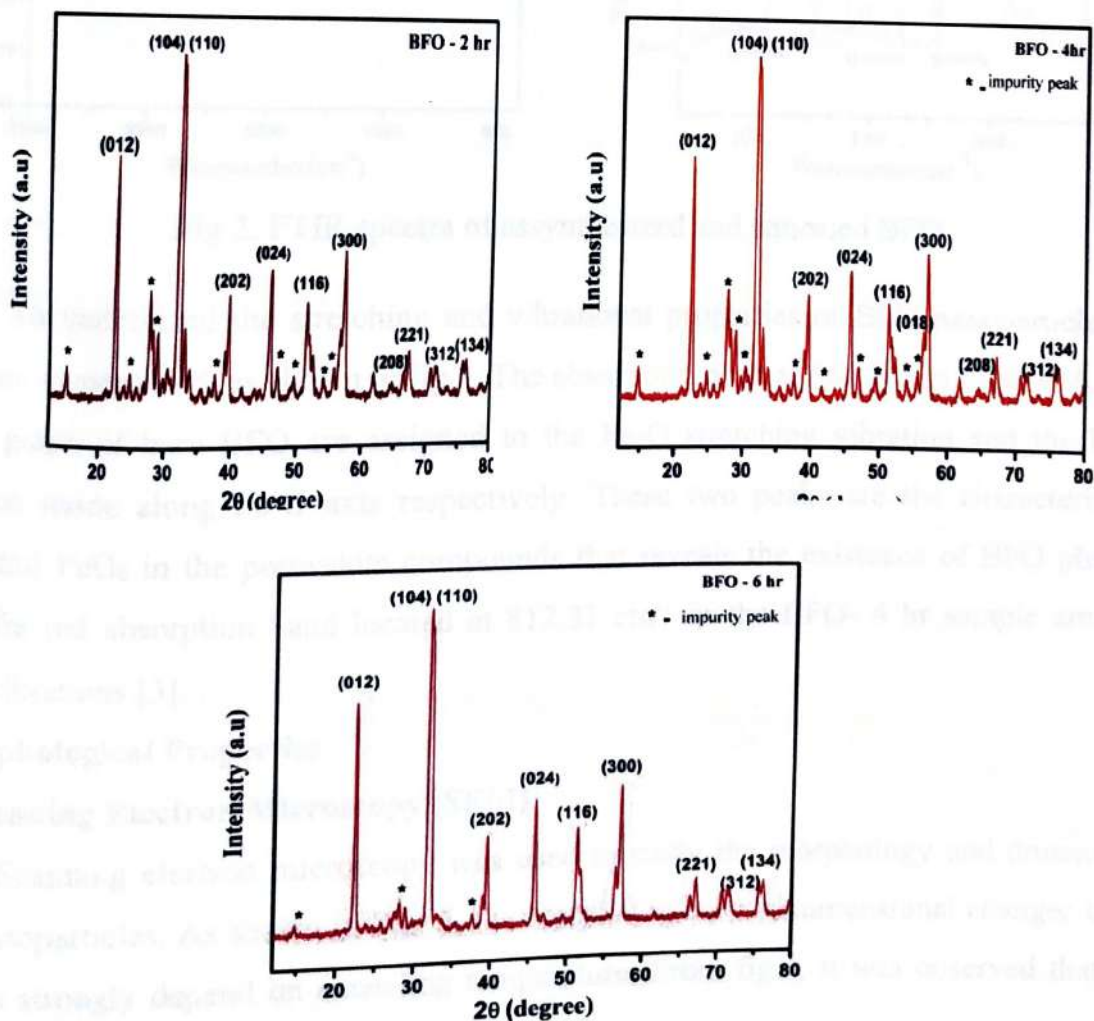


Fig 1: XRD pattern of as synthesized BFO nanoparticles annealed at different temperature.

1.2) FTIR Spectroscopy (FT-IR)

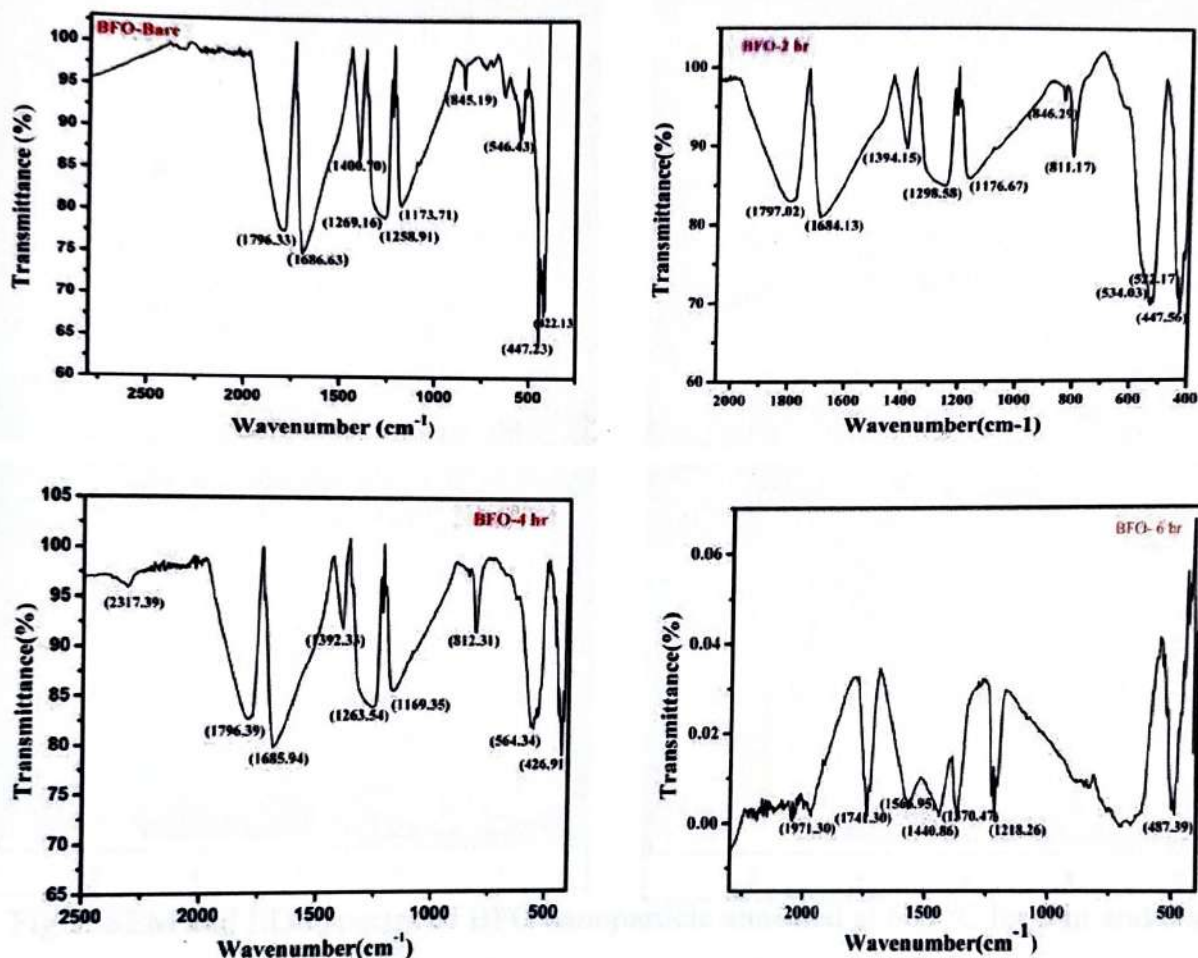


Fig 2: FTIR spectra of assynthesized and annealed BFO

To understand the stretching and vibrational properties of BFO nanoparticles FTIR spectrum is measured, as shown in fig.2. The absorption peak at 564.34 cm^{-1} and 426.91 cm^{-1} in the graph of bare BFO are assigned to the Fe-O stretching vibration and the bending vibration mode along Fe-O axis respectively. These two peaks are the characteristics of octahedral FeO_6 in the perovskite compounds that reveals the existence of BFO phase [2]. The infra red absorption band located at 812.31 cm^{-1} in the BFO- 4 hr sample are due to NO_3^{-1} vibrations [3].

2) Morphological Properties

2.1) Scanning Electron Microscopy (SEM)

Scanning electron microscopy was used to study the morphology and dimension of BFO nanoparticles. As shown in Fig. 3, the morphological and dimensional changes in BFO powders strongly depend on annealing temperature. From fig.3, it was observed that, BFO

powder exhibit nearly spherical microstructure. It was also observed that, the particles were in agglomerated form with non uniform distribution.

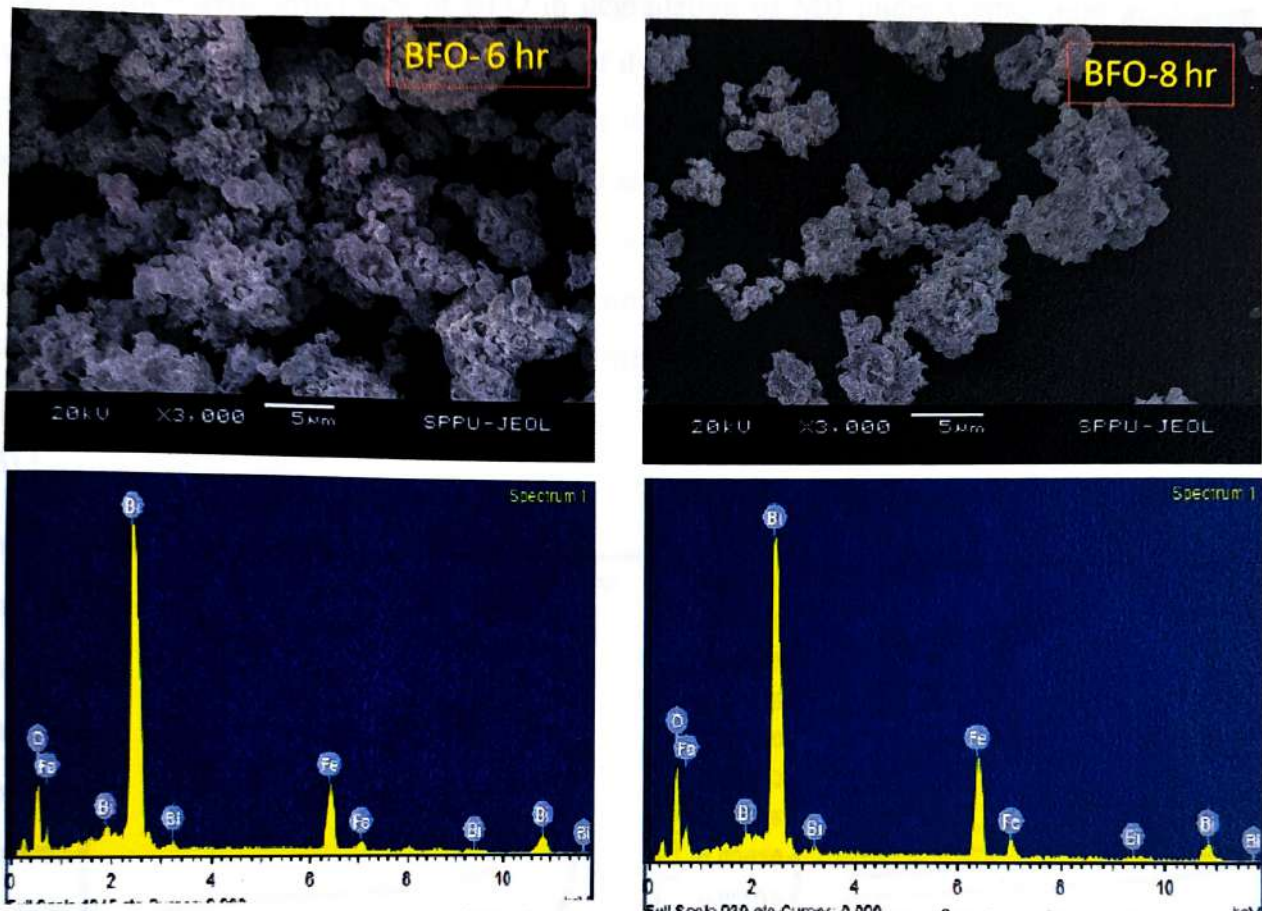


Fig 3: SEM and EDS spectra of BFO nanoparticle annealed at 600 °C for 6 hr and 8 hr

3) Photocatalytic activity of BFO

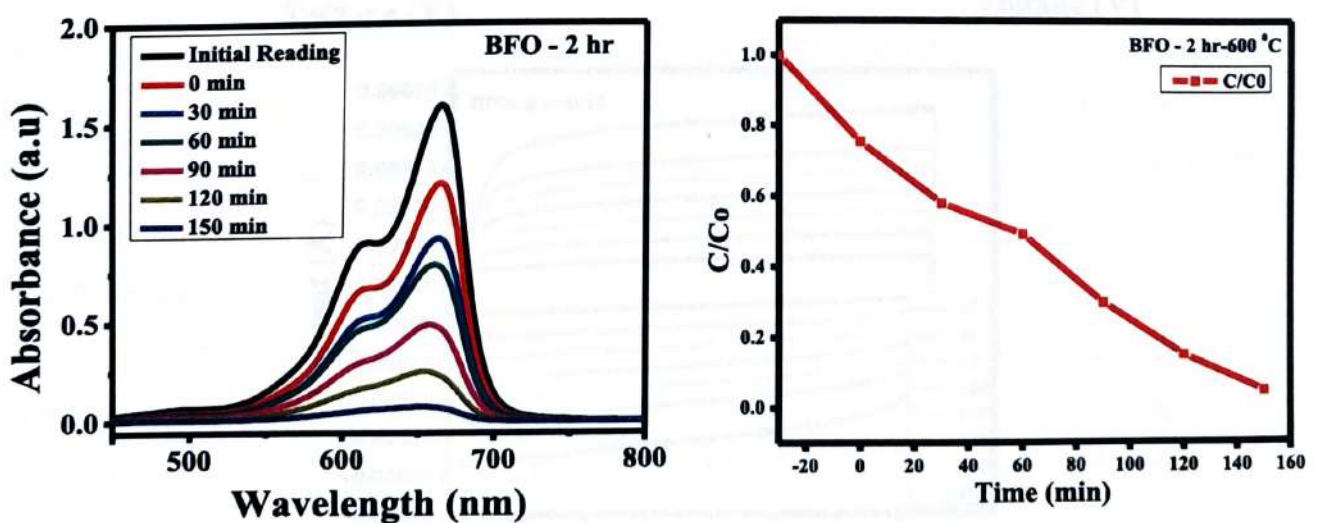
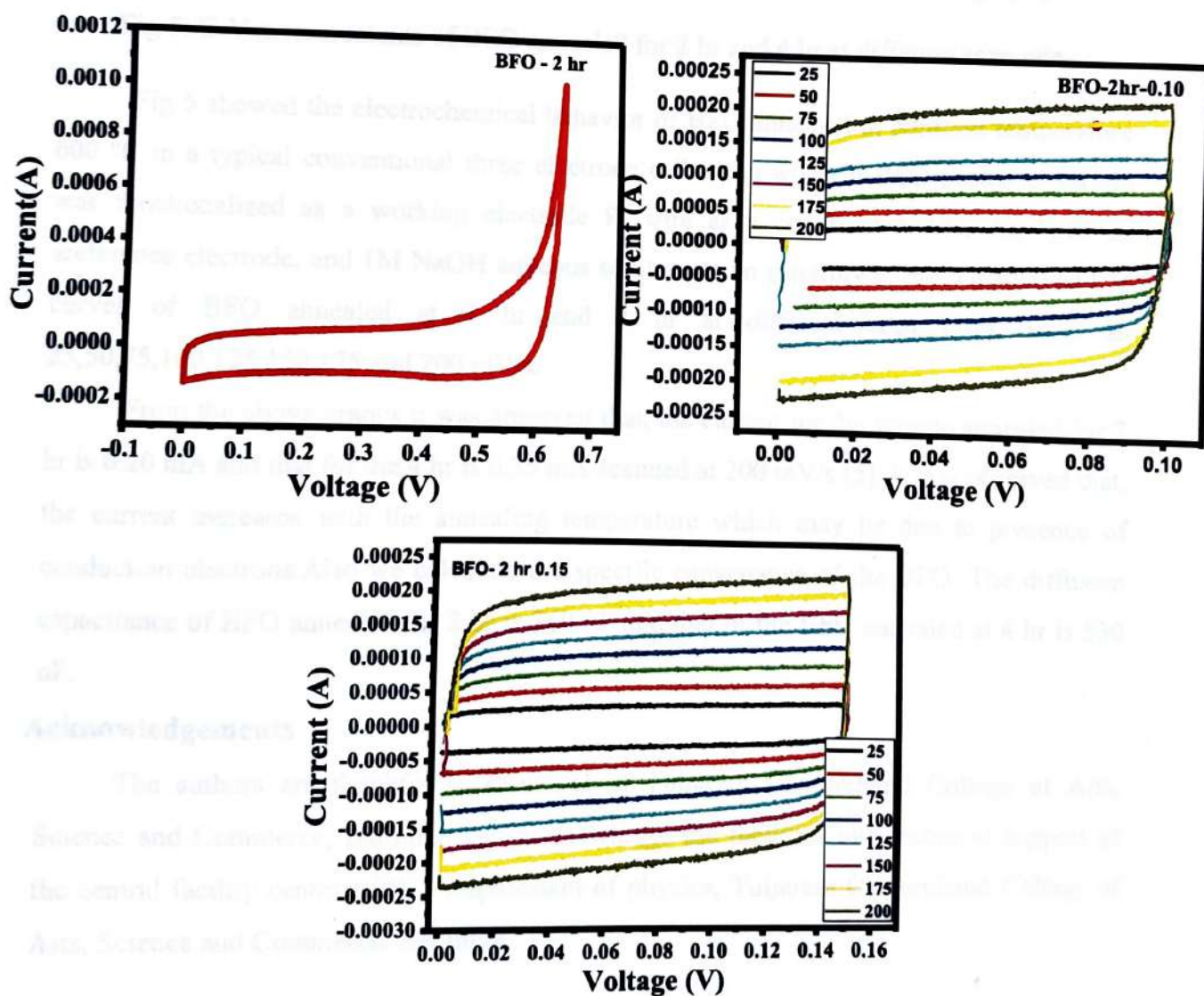


Fig 4: Photocatalytic activity of BFO nanoparticles annealed at 600 °C for 2 hr

The photocatalytic activity of BiFeO₃ nanoparticles were studied via photocatalytic degradation of methylene blue (MB) dye in an aqueous solution under visible light irradiation.

MB dye was selected as a typical pollutant because of its obvious absorption at 663 nm. The photocatalytic degradation experiments were performed using MB in presence of BFO photo catalyst while maintaining pH value at 3 and the results were presented in fig 4. The photocatalytic efficiency of BFO in degradation of MB under visible light irradiation was determined with initial concentration of dye at 50 mg/L and catalyst loading of 0.1 g/L. The rapid decrease of MB absorption at the wavelength of 663 nm indicates breakdown of MB. The photo degradation of MB for BFO as a photocatalyst under visible light irradiation by the C/Co ratio graph is shown in Fig. 4 above. The initial concentration was Co and C which was concentration at the time t. From fig 4, It was clear that, the BFO particles annealed at 600 °C degraded 95 % of the MB, respectively after 150 min, which is quite good as compared to the reported values [4].

5) C-V Measurements



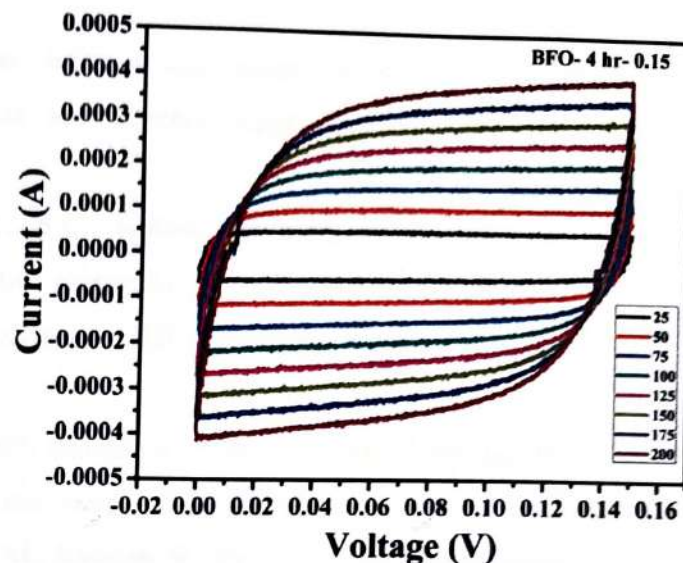
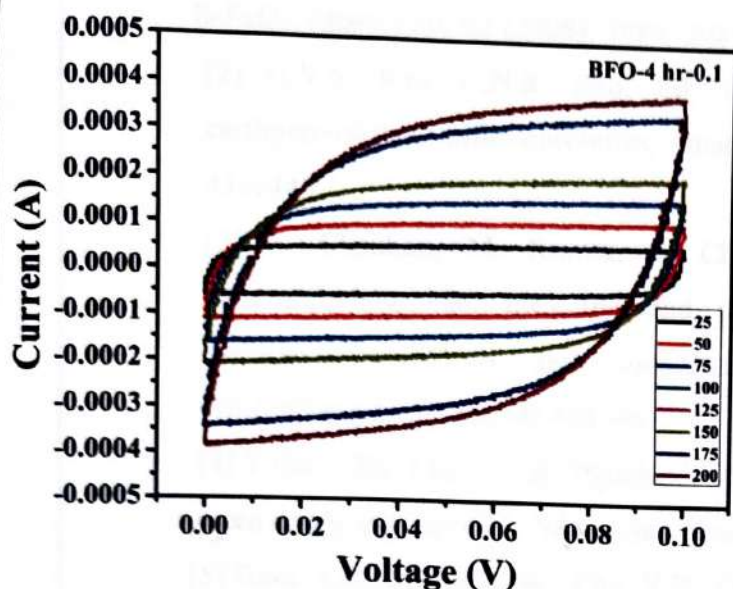


Fig 5: C-V measurements of BFO annealed for 2 hr and 4 hr at different scan rate

Fig 5 showed the electrochemical behavior of BFO annealed at constant temperature 600°C in a typical conventional three electrode cell setup wherein BFO coated electrode was functionalized as a working electrode Pt wire as a counterelectrode, Ag/AgCl as a reference electrode, and 1M NaOH aqueous solution as an electrolyte. Fig 5 displayed CV curves of BFO annealed at 2 hr and 4 hr at different scan rates, such as 25, 50, 75, 100, 125, 150, 175 and 200 mV/s.

From the above graphs it was observed that, the current for the sample annealed for 2 hr is 0.20 mA and that for the 4 hr is 0.35 mA scanned at 200 mV/s [5]. It was observed that, the current increases with the annealing temperature which may be due to presence of conduction electrons. Also we calculate the specific capacitance of the BFO. The diffusion capacitance of BFO annealed for 2 hr is 360 nF and that of the BFO annealed at 4 hr is 530 nF.

Acknowledgements

The authors are thankful to Principal of Tuljaram Chaturchand College of Arts, Science and Commerce, Baramati and acknowledge the facilities and technical support of the central facility center (CFC), Department of physics, Tuljaram Chaturchand College of Arts, Science and Commerce, Baramati.

References

- [1] T. Carvalho and P. Tavares, *Synthesis and thermodynamic stability of multiferroic BiFeO₃*, Mater Lett, 62 (2008), 3984–3986.
- [2] G.V.S. Rao, C.N.R. Rao, J.R. Ferraro, Infrared and electronic spectra of rare earthperovskites: ortho-chromites, -manganites and -ferrites, Appl. Spectrosc. 24(1970) 436e445.
- [3] S. Chauhan, M. Kumar, S. Chhoker, S.C. Katyal, A comparative study on structural,vibrational, dielectric and magnetic properties of microcrystalline BiFeO₃, nanocrystallineBiFeO₃ and core-shell structured BiFeO₃@SiO₂ nanoparticles, J. AlloysCompd. 666 (2016) 454–467.
- [4] T Gao , Zhi Chen, et al, “Synthesis of BiFeO₃ nanoparticles for the visible-light induced photo catalytic property”, J. Materials Research Bulletin 59, 6–12, (2014).
- [5] Basu, S.R., Martin, L.W., Chu, Y.H., Gajek, M., Ramesh, R., Rai, R.C., Xu, X., Musfeldt, J.L., 2008. Photoconductivity in BiFeO₃ thin films. Appl. Phys. Lett. 92, 091905.

Chapter- V

Summary and Conclusions

In summary we synthesize the BiFeO_3 nanoparticles annealed at constant temperature 600°C for 2 hr, 4 hr, 6 hr and 8 hr respectively by sol-gel method which is a fast and economic method with a high production rate. The synthesized nanoparticles can be used as a catalyst for electrochemical water splitting. It was observed that, annealing time shown obvious influence on structural, morphological, photocatalytic and electro catalytic activity of the sample.

The XRD patterns revealed that all the prepared BFO nanoparticles were crystalline and crystallinity increased with annealing time. SEM micrographs shown that inhomogeneous distribution of BFO nanoparticles which are in agglomerated form and had nearly spherical morphology with average particle size nearly $60\text{ }\mu\text{m}$. The degradation efficiency of pollutant in the presence of BFO was anticipated through calculation of band position and a number of experiments. The produced hydroxyl radicals from the photo generated electron hole pairs through chain reactions were the major reactive species, and finally resulted in proficient pollutant degradation. However the electro catalytic activity of BFO catalyst was limited due to their poor charge separation efficiency and unfavorable surface kinetics.

Acknowledgements

The authors are thankful to Principal of Tuljaram Chaturchand College of Arts, Science and Commerce, Baramati and acknowledge the facilities and technical support of the central facility center (CFC), Department of physics, Tuljaram Chaturchand College of Arts, Science and Commerce, Baramati. We are happy to share that, we have published a patent for design titled "Photoelectrochemical Water Splitting Reactor". (Design no: 6354209, Grant date: 29 March 20240)



Intellectual
Property
Office

Certificate of Registration for a UK Design

Design number: 6354209

Grant date: 29 March 2024

Registration date: 21 March 2024

This is to certify that,

in pursuance of and subject to the provision of Registered Designs Act 1949, the design of which a representation or specimen is attached, had been registered as of the date of registration shown above in the name of

Dr. KALANGE ASHOK EKANATH, Dr. KULKARNI SACHIN BABASAHEB, Mr.

THORAT SOPAN MURALIDHAR

in respect of the application of such design to:

Photoelectrochemical Water Splitting Reactor

International Design Classification:

Version: 14-2023

Class: 24 MEDICAL AND LABORATORY EQUIPMENT

Subclass: 01 APPARATUS AND EQUIPMENT FOR DOCTORS, HOSPITALS
AND LABORATORIES

Adam Williams

Comptroller-General of Patents, Designs and Trade Marks

Intellectual Property Office

The attention of the Proprietor(s) is drawn to the important notes overleaf.



Intellectual Property Office is an operating name of the Patent Office

IP/24/000000